Remote Sensing of Environment 263 (2021) 112557

Contents lists available at ScienceDirect

Remote Sensing of Environment

journal homepage: www.elsevier.com/locate/rse

Quantifying uncertainties in nighttime light retrievals from Suomi-NPP and NOAA-20 VIIRS Day/Night Band data

Zhuosen Wang [a,b,*], Miguel O. Román [c], Virginia L. Kalb [b], Steven D. Miller [d], Jianglong Zhang [e], Ranjay M. Shrestha [f,b]

[a] Earth System Science Interdisciplinary Center, University of Maryland College Park, College Park,MD, USA
[b] Terrestrial Information Systems Laboratory, NASA Goddard Space Flight Center, Greenbelt, MD,USA
[c] Earth from Space Institute, Universities Space Research Association, Columbia, MD, USA
[d] Cooperative Institute for Research in the Atmosphere, Colorado State University, Fort Collins, CO, USA
[e] Department of Atmospheric Sciences, University of North Dakota, Grand Forks, ND, USA
[f] Science Systems and Applications, Inc., Lanham, MD, USA

ARTICLE INFO

Editor: Dr Marie Weiss

ABSTRACT

Satellite observations of nighttime lights (NTL) from Suomi-NPP and NOAA-20 VIIRS Day/Night Band data have been widely used to estimate human activities. Long-term changes such as urban development and abrupt short-term changes such as power outages have been monitored from temporal NTL acquired by satellites. While high temporal NTL variation has been found across NTL data of varying temporal scale (e.g., daily, monthly, and annual composites), the sources of measurement error and uncertainty are poorly understood. This paper quantifies the sources of VIIRS-derived NTL uncertainty due to view-illumination geometry, surface Bidirectional Reflectance Distribution Function (BRDF)/albedo, and the effects of snow cover, lunar irradiance, aerosol loading, cloud mask, vegetation, geometry, and ephemeral artifacts (e.g., the Aurora Borealis). Based on this current assessment of NASA Black Marble retrievals (VNP46, Collection V001), we found that angular and atmospheric effects dominate retrieval uncertainty. Errors introduced by upstream data inputs (e.g., a coarser nighttime snow cover flag and misclassification errors in the existing VIIRS nighttime cloud mask) were also found to impact retrieval quality. Despite these challenges, a consistent daily NTL time series record can be routinely generated from top-of-atmosphere VNP46 radiances. Key recommendations include: (1) the use of lunar-BRDF adjusted and atmospherically corrected NTL (i.e., as identified as high-quality retrievals in the VNP46 QA fields), (2) development and improvement to the VIIRS snow cover and cloud masks algorithms to accurately reflect NTL retrieval conditions, (3) characterizing seasonal variations in NTL due to vegetation and snow, (4) reducing geometric effects due to the spatial mismatch of gridded pixel and observation footprint, (5) employing angularly-consistent NTL observations from multiple VIIRS instruments (i.e., Suomi-NPP and NOAA-20) to reduce pixel-based uncertainties and address persistent data gaps, and (6) being mindful of surface-reflected radiance from aurora events at mid-to-high latitudes.

1. Introduction

Nighttime light (NTL) observations acquired by satellites are a crucial indicator of human activities. Recent studies have employed statistical analyses and correlation discovery methods to establish the relationships between NTL and a wide range of human-linked patterns and processes. Such findings are of immediate relevance to the United Nations Program on Urban Sustainable Development Goals (SDGs) of the 2030 Agenda (https://sdgs.un.org/goals), which aims to reduce poverty, fight inequalities and injustice, and protect the environment. Parameters relevant to these objectives include a multitude of socio-economic variables (e.g. population, GDP, poverty, house vacancy rate) (Chen and Nordhaus, 2015; Chen et al., 2015; Jean et al., 2016; Levin and Zhang, 2017; Li et al., 2013b; Liu et al., 2019; Ma et al., 2020, 2014; Shi et al., 2014b; Yu et al., 2015), environmental variables (e.g. carbon emissions, PM2.5 concentration, light pollution) (Bennie et al., 2015; Gaston et al., 2013; Jiang et al., 2018, 2017b; Li et al., 2017b; Oda and Maksyutov, 2011; Ou et al., 2015; Wang et al., 2016), tracking urban

---

* Corresponding author at: Earth System Science Interdisciplinary Center, University of Maryland College Park, College Park, MD, USA.
E-mail address: zhuosen.wang@nasa.gov (Z. Wang).

https://doi.org/10.1016/j.rse.2021.112557
Received 20 November 2020; Received in revised form 2 June 2021; Accepted 7 June 2021

extent (Guo et al., 2015; Sharma et al., 2016; Shi et al., 2014a; Zhou et al., 2014), disaster impacts (Li et al., 2018b; Román et al., 2019; Wang et al., 2018a; Zhao et al., 2018), energy consumption (Amaral et al., 2005; Coscieme et al., 2014; Román and Stokes, 2015), crime rates (Liu et al., 2020b; Zhou et al., 2019), conflict (Jiang et al., 2017a; Levin et al., 2019; Li et al., 2018a, 2017a, 2013a; Li and Li, 2014; Witmer, 2015), health-related issues (Cho et al., 2015; Elvidge et al., 2020; Liu et al., 2020a), and characterizing spatial features e.g., upper-atmospheric gravity waves (Miller et al., 2015; Hu et al., 2019), fishing vessels (Elvidge et al., 2015), gas flares (Elvidge et al., 2009), and nighttime fires (Wang et al., 2020a).

A consistent temporal NTL record is required to quantitatively analyze human activities from regional to global scales. The Defense Meteorological Satellite Program's Operational Line Scanner *(*DMSP/OLS) has collected NTL imagery since the late 1960's, and continues today in the final members of that pioneering constellation (Elvidge et al., 1997). However, the quality of original DMSP/OLS NTL data is known to be poor due to the lack of onboard calibration, coarse radiometric resolution (6-bit), sensor degradation, blooming effect, and saturation over bright regions (Wu et al., 2013; Zhang et al., 2013, 2016; Zhao et al., 2020; Zheng et al., 2019, 2020). Radiance calibrated DMSP/OLS NTL have been generated by combining low and high gain composites for seven discrete years (Elvidge et al., 1999). While several studies have sought to improve these techniques, long-standing data provenance and access issues have prevented researchers from conducting uncertainty assessments that combine such data sources. In particular, the lack of a daily radiance-calibrated DMSP/OLS data record (Level-1B equivalent) has prevented the reproducibility of published studies and retrieval techniques involving DMSP/OLS data (Levin et al., 2020).

A new generation of NTL observations is now available from the Visible Infrared Imaging Radiometer Suite (VIIRS) Day/Night Band (DNB) (Miller et al., 2012, 2013), a visible/near-infrared (500-900 nm) broadband radiometer onboard the Suomi-National Polar-orbiting Partnership (S-NPP). The DNB has observed NTL since late 2011 with vastly improved performance compared to the OLS in terms of calibration and higher spatial resolution (750 m) (Miller et al., 2013; Lee et al., 2015; Liao et al., 2013; Xiong et al., 2014). VIIRS, drawing heritage from the OLS, the Advanced High-Resolution Radiometer (AVHRR), and the Moderate-resolution Imaging Spectroradiometer (MODIS), is a combined mission of NASA and NOAA. NOAA-20, launched in 2017, carries the same VIIRS instrument as S-NPP. The stray light corrected VIIRS DNB is temporally stable and calibrated with high accuracy (Cao et al., 2019; Cao and Bai, 2014; Lee et al., 2015; Shao et al., 2013; Wang and Cao, 2016). Several other satellites have recently launched, such as Jilin-1 and Luojia-1 (Guk and Levin, 2020; Levin et al., 2020; Li et al., 2018c), providing high spatial resolution NTL imagery. The local overpass times of DMSP/OLS, VIIRS/DNB, and Luojia-1 are approximately 7:30 pm, 1:30 am, and 10:00 pm respectively, limiting direct inter-comparison among these platforms considering the high NTL diurnal variation (Li et al., 2020).

High variation in satellite-derived NTL time series, including temporally-smoothed monthly NTL composites, can impact the use of these products for science and application development (Coesfeld et al., 2018; Levin et al., 2020). Therefore, quantifying sources of measurement error and retrieval uncertainty is crucial to ensure the usability of the derived products (Solbrig et al., 2020; Coesfeld et al., 2018). For instance, NTL radiance's non-linear relationship with view angle depends highly on land use (Li et al., 2019; Tong et al., 2020), which can have a major impact on studies addressing linkages between urban growth and socioeconomic indicators (Stokes and Seto, 2019). NTL radiance has been shown to increase toward higher View Zenith Angles (VZA), the angle between the line of sight to the satellite and local zenith (the line directly above the point on the ground), over residential areas, while the opposite trend is often found across dense urban centers (Li et al., 2019). Likewise, surface-reflected lunar radiance (herby termed the 'Lunar BRDF' effect) can increase the magnitude of NTL by several orders of magnitude (Román et al., 2018). Consequently, monthly and annual VIIRS NTL composites (e.g., those released by Payne Institute at Colorado School of Mines) have been composited from moon-free night observations only, ignoring the lunar BRDF effect (Elvidge et al., 2017). This exclusion reduces the number of available high-quality clear-sky observations (by ~50%) for near-real-time uses of NTL data. It also impacts the composited results' overall quality, particularly across persistently cloudy regions (e.g., in the tropics), where moon-free retrievals are more prone to retrieval uncertainties.

NTL radiance is sensitive to aerosol and is negatively correlated with aerosol loadings (Zhang et al., 2019; Wang et al., 2020). Because of the broad spectral range of the VIIRS DNB, high aerosol loadings reduce urban NTL radiance, while enhancing the radiance over natural and low light areas adjacent to dense urban centers (Sanchez de Miguel et al., 2020; Tong et al., 2020). Nighttime cloud masking using VIIRS is also a major challenge. The accuracy of the VIIRS nighttime cloud detections (global hit rate of 94%) is relatively lower than daytime estimates (Kopp et al., 2014). These upstream errors are amplified in the NTL retrieval process, as cloud-contaminated NTL pixels, both within and nearby cloudy areas can reduce and enhance the upwelling surface NTL during moon-free and moonlit nights, respectively. Airglow brightness is highly variable spatially and temporally (Miller et al., 2012; Coesfeld et al., 2020). The airglow radiance ranges from 0.1 to 1.0 nWcm^{-2} sr^{-1} μm^{-1} viewed from the surface at local zenith (Hofmann et al., 1977). Coesfeld et al. (2020) corrected the airglow natural light for VIIRS DNB, which is mostly less than 0.5 nWcm^{-2} sr^{-1} and mainly influences natural areas while has little impact on urban areas.

The presence of nighttime snow also enhances the scattering of reflected NTL and lunar radiance (Román and Stokes, 2015; Levin, 2017). As with nighttime cloud-detection, snow detection at night using VIIRS is challenging because of the lack of multispectral measurements and the higher-order scattering effects that enhance the magnitude of nearby snow-free NTL pixels over hilly and mountainous regions. Moreover, the current VIIRS Collection V001 products use a nighttime snow flag (25 km) measured by Special Sensor Microwave Imager/Sounder (SSMIS) onboard DMSP (Armstrong and Brodzik, 2001) from the National Snow & Ice Data Center's (NSIDC), which is much coarser than the native 750 m VIIRS DNB spatial footprint (Armstrong and Brodzik, 2001), and the existing standard VIIRS snow products (VNP10) available at 375 m (Riggs et al., 2017).

Vegetation phenology-related NTL artifacts are another key source of measurement error (Levin, 2017; Xie et al., 2019; Zheng et al., 2019). The magnitude of surface light penetrates vegetation canopy depending on gap fraction (Román et al., 2018). This seasonal occlusion effect is thus stronger during leaf-on periods in late spring and summer months compared to leaf-off periods in the fall and winter months.

The spatial coverage of gridded VIIRS pixel does not match well with the actual satellite observation footprint, which depends on gridded pixel size, observation spatial footprint, point spread function, and view angles (Tan et al., 2006; Campagnolo et al., 2016). The spatial mismatch can impact the temporal consistency of NTL radiance particularly over areas with abrupt boundaries.

NTL radiance at mid-to-high latitude regions could be affected by ephemeral aurora (Seaman and Miller, 2013). NTL radiance within one aurora oval varies dramatically. The reflected aurora radiance from nearby Earth surface without aurora above the sky is difficult to be corrected since the downwelling aurora irradiance is unknown. These effects are compounded by sub-optimal retrievals conditions, including residual instrument straylight artifacts, and the presence of the twilight region, where the VIIRS DNB exhibits lower solar zenith angles regimes ($SZA < 108^\circ$) for extended periods of time, particularly in the midsummer months.

Regardless of a product's temporal frequency (daily vs. monthly or annual composited data) or index used (e.g., Radiance vs. Sum Of Lights, 'SoL'), users also need to be aware that calibration stability and consistency are essential to ensure a science-quality NTL time series, and to make key conclusions based on their results. For instance, the early NOAA VIIRS Sensor Data Record's (SDR) operational DNB calibration was inconsistent in calibration coefficients, Relative Spectral Response (RSR), stray light correction, atmospheric airglow contamination, and striping for higher aggregation zones (Cao et al., 2021). The radiometric accuracy was also reduced by more than 10% at a low radiance level (affecting rural NTL populations) due to the airglow contamination in dark offset (Cao et al., 2021; Uprety et al., 2019). Higher-order monthly and annual VIIRS NTL composite products derived from these data (e.g., those currently available via Google Earth Engine and AWS as of April 2021) have yet to be reprocessed and updated. Conversely, NASA's Land Science Investigator-led Processing System has conducted two comprehensive data reprocessing campaigns (Collections V001-V002) for all Level 1–3 VIIRS sensor data and higher-order products (e.g., Black Marble – VNP46) spanning the entire mission period (Jan 19, 2012 – YTD.)

It is also important to note that Day/Night Visible Imagery, e.g. the VIIRS Day/Night Band, Enhanced Near Constant Contrast (ENCC) layer available through https://worldview.earthdata.nasa.gov/, is mainly a qualitative product and should be strictly used for image display purposes. For this layer, each VIIRS Level 1B scan (6-min in total length) is individually processed and normalized based on a static set of values that predict the viewing and illumination geometries of each pixel. Because of the confounding factors that influence a VIIRS scan from one night to the next (e.g., more/less cloudy days, with more/less moon illumination conditions), individual ENCC pixel-based values are not comparable over time. For accurate time-series detection (e.g., monitoring short-term increases or reductions in artificial lights at night), users are referred to NASA's Black Marble standard product suite (VNP46A1/VNP46A2 for Suomi-NPP). These standard products correct for short-term variations in lunar and environmental conditions. They also provide the necessary quality assurance (QA) flags and additional layers to identify and isolate potential sources of noise and measurement error (e.g., clouds, moonlight, and snow contaminated pixels) and variations (e.g. lunar and view angles and view time) in a statistically robust fashion.

Accordingly, this paper aims to characterize the magnitude and extent of NTL uncertainties that arise from natural and extraneous sources and sinks of NTL emissions. Section 2 describes the datasets and methodology. The uncertainty of each factor is analyzed in Section 3. Section 4 discusses the contribution and coupled effects of these factors and potential solutions to characterize and reduce higher-order NTL uncertainty.

2. Datasets and methodology

2.1. Datasets

NTL data from the NASA's daily Black Marble products suite (VNP46) are used for quantifying radiance as functions of observing conditions in this study. To assist the analysis, four other datasets including NASA VIIRS BRDF/albedo product (VNP43), AERONET (Aerosol Robotic NETwork), Luojia-1 satellite imagery, and Los Angeles Region Imagery Acquisition Consortium (LARIAC), are also used.

NASA's Black Marble products suite (VNP46; Román et al., 2018) consists of Top-of-Atmosphere (TOA) DNB radiance along with ancillary data on the solar, lunar and viewing geometry, scene brightness temperature, cloud, snow, moon illumination fraction, moon phase, view time, glint angle, and quality flags (VNP46A1), lunar BRDF-corrected radiance (VNP46A2), and monthly and annual composite radiance (VNP46A3/4). Gap-filled radiance and adjusted cloud and snow mask during surface NTL retrieval are also provided in VNP46A2. Black Marble products minimize the extraneous noise by performing a novel "*Turning off the Moon*" and atmospheric correction retrieval strategy. Reflected lunar radiance is estimated and removed by integrating surface BRDF/Albedo acquired from VIIRS BRDF/albedo product (VNP43) (Liu et al., 2017; Schaaf et al., 2002; Wang et al., 2018b) and a lunar irradiance model (Miller and Turner, 2009). Atmospheric correction is performed by the vector radiative transfer modeling (Román et al., 2018). A daily change of 0.43 nWcm^{-2} sr^{-1} can be successfully detected by Black Marble product (Román et al., 2018).

NASA VIIRS BRDF/albedo product (VNP43) was retrieved with the RossThick-LiSparse Reciprocal (RTLSR) model (Liu et al., 2017; Schaaf et al., 2002; Wang et al., 2018b). RTLSR model was fitted with 16 days of clear sky multi-angular surface reflectance weighted by retrieval quality and temporal proximity to the day of interest to retrieve surface BRDF/albedo.

The vegetation effect on NTL was evaluated using Normalized Difference Vegetation Index (NDVI), derived from VIIRS Nadir BRDF-Adjusted Reflectance (NBAR) (VNP43A4). The NASA products (VNP46 and VNP43) were downloaded from NASA DAAC (earthdata.nasa.gov/eosdis/daacs).

Surface based observations were leveraged for evaluation of aerosol effects. The AERONET (Aerosol Robotic NETwork), established by NASA and PHOTONS (PHOtométrie pour le Traitement Opérationnel de Normalisation Satellitaire), is a globally distributed and long-term ground-based networks providing high-precision measurements of aerosol properties (Giles et al., 2019a). Nighttime Aerosol Optical Depth (AOD) was retrieved from lunar photometer measurements and available during moonlit nights (Barreto et al., 2019; Berkoff et al., 2011; Giles et al., 2019b). Level 1.5 (cloud-screened and quality-controlled) daytime and nighttime AOD were downloaded from the NASA AERONET site (https://aeronet.gsfc.nasa.gov/).

The Luojia-1 satellite, launched in June 2018, acquires 130 m spatial resolution nighttime low-light imagery (including NTL) through a panchromatic band (460-980 nm) developed at Wuhan University (Li et al., 2018c). The revisit period is 15 days with a local overpass time approximate 10:00 pm. The radiometrically calibrated nighttime light imageries were downloaded from the Luojia-1 satellite webpage (http://59.175.109.173:8888) to evaluate the geometric effect on DNB NTL uncertainty. The footprint of DNB observations is not the same as the grid pixel coverage. The footprint of DNB observations acquired at different times within the same grid pixel is also not the same.

Building heights over Los Angeles acquired from Los Angeles Region Imagery Acquisition Consortium (LARIAC) (https://lariac-lacounty.hub.arcgis.com/) were compared with annual nighttime radiance to evaluate the angular-viewing effect on NTL. The building heights were estimated from stereo imagery with approximately nominal 10 cm and 28 cm GSD (Ground Sample Distance). The height shapefile was re-projected to geographic linear latitude longitude to match with nighttime radiance.

2.2. Study area

Twenty-four globally-distributed sites in seven metropolitan areas representing a gradient of commercial urban center – residential – rural areas with different vegetation conditions and building heights were selected to evaluate NTL radiance uncertainty (Fig. 1, Table 1). No obvious land cover/land use changes were observed from google earth historical images over these selected locations during the study period. Commercial centers with different building heights were chosen to evaluate the impact of urban 3D infrastructure structure. The building heights of Beijing and Rome's old town sites are much lower than other commercial center locations.

Thirty-seven globally-distributed AERONET sites offering both daytime and nighttime AOD measurements were chosen to evaluate the aerosol effect (Fig. 1, Table 2). The land use of these sites ranges from natural areas, villages, small towns, middle towns, city edge to big cities.

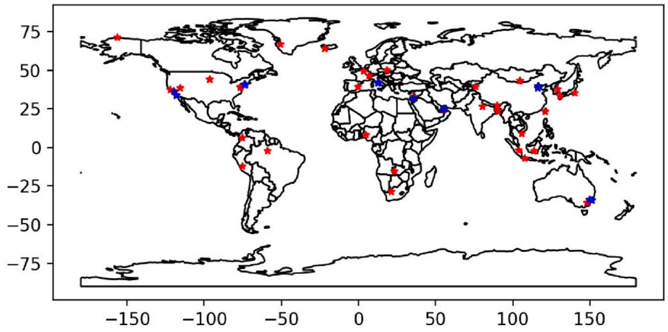

Fig. 1. Spatial distribution of chosen AERONET sites (red) and nighttime artificial light locations (blue). (For interpretation of the references to colour in this figure legend, the reader is referred to the web version of this article.)

2.3. *Metrics to quantify the uncertainty*

To quantify uncertainties in NTL radiances, a few metrics are used, including coefficient of variation (CV), relative change, radiance-view zenith quadratic model, normalized difference between Hotspot and Darkspot NTL radiance ($NDHD_{NTL}$), and semivariogram.

(1) Coefficient of Variation (CV):

$$CV = \frac{SD}{\overline{X}} \tag{1}$$

Where *SD* represents Standard Deviation, $\overline{X}$ is the mean value. *CV* is a standardized measure of dispersion of the dataset. It indicates the relative variability and allows the comparison of two datasets with different scoring mechanisms. CV is calculated from daily lunar BRDF-corrected NTL radiance.

(2) Relative change:

$$RC = \left(\frac{NTL_{TOA} - NTL_{surface}}{NTL_{surface}}\right)*100\% \tag{2}$$

Where NTL_{TOA} represents top-of-atmosphere NTL radiance, $NTL_{surface}$ is surface bottom-of-atmosphere NTL value.

$$RC_a = \left(\frac{NTL_{ma} - NTL_{ca}}{NTL_{ca}}\right)*100\% \tag{3}$$

Eq. (3) was used to estimate the relative change with different lunar irradiance in Section 3.7. NTL_{ma} is the retrieved surface NTL using an misused surface albedo (e.g., snow albedo for snow-free surface). NTL_{ca} represents the surface NTL using correct albedo.

(3) Radiance-view zenith quadratic model:

$$R = ax^2 + bx + c \tag{4}$$

Where *R* represents lunar BRDF-corrected radiance, *x* is VZA. The highest/lowest NTL is located at $-b/(2a)$ VZA.

(4) Normalized Difference between Hotspot and Darkspot NTL radiance ($NDHD_{NTL}$):

$NDHD_{NTL}$ is implemented in the study as an angular index to characterize the surface anisotropic features and has been used to estimate vegetation canopy structure in some past studies (Chen et al., 2005; Wei and Fang, 2016).

$$NDHD_{NTL} = \frac{(NTL_{hotspot} - NTL_{darkspot})}{(NTL_{hotspot} + NTL_{darkspot})} \tag{5}$$

Here $NDHD_{NTL}$ was utilized to estimate the angular characteristics of lunar BRDF-corrected NTL along with view angles. VZA was grouped into seven bins (0–10, 10–20, 20–30, 30–40, 40–50, 50–60, and 60–70 degree). $NTL_{hotspot}$ is the highest radiance of the VZA bins and $NTL_{darkspot}$ represents the lowest radiance.

(5) Semivariogram:

Semivariogram has been used to describe surface heterogeneity (Román et al., 2009; Wang et al., 2012, 2014).

$$\gamma_E(h) = 0.5\frac{\sum_{i-1}(Z_{xi} - Z_{xi+h})^2}{N(h)} \tag{6}$$

Where $\gamma_E(h)$ is the semivariogram between lunar BRDF-corrected NTL radiance within a certain distance *h*. *N(h)* represents the number of paired pixels at a distance of *h*. Z_{xi} is the NTL radiance at pixel *x* and Z_{xi+h} is the radiance of the paired pixel index *i*. Semivariogram is then fitted to a spherical model to estimate spatial attributes (Román et al., 2009; Wang et al., 2012).

$$\gamma_{sph}(h) = \begin{cases} c_0 + c\cdot\left(1.5\frac{h}{a} - 0.5\left(\frac{h}{a}\right)^3\right) & for\, 0 \le h \le a \\ c_0 + c & for\, h > a \end{cases} \tag{7}$$

Sill value (*c*) is the maximum semivariance fitting the spherical model and range (*a*) represents the distance *h* at which semivariogram reaches an asymptote. Range describes the distance with no further correlation of NTL radiance associated with a point. c_0 (nugget) indicates the semivariogram value at $h = 0$.

The results for surface BRDF/albedo and AOD related NTL uncertainty analysis such as atmospheric, surface BRDF/albedo, snow, and cloud effects were simulated by the radiative transfer atmospheric correction model (Román et al., 2018).

3. Factors impacting NTL uncertainty

This paper mainly focuses on the NTL uncertainty corresponding to external factors such as view-angle, snow, aerosol, cloud, geometric, lunar irradiance, surface BRDF/albedo, vegetation, and aurora. NTL radiance variation due to human activities (Román and Stokes, 2015) is not discussed in this study. We found that NTL radiance exhibited strong heterogeneity with large varying spatial range. To reduce the geometric effect, discussed in Section 3.8, the average NTL radiance from a 3 by 3 pixels window was used to evaluate the uncertainty corresponding to angular, aerosol, lunar, and vegetation effects.

3.1. *Angular effect*

Upwelling light measured by the DNB at night is composed primarily of direct light from artificial (e.g. street lamps, vehicle headlight, indoor light through a window), reflected light from neighboring light sources, and reflected lunar radiance. Reflected lights depend on land surface BRDF/albedo, which is anisotropic (Schaaf et al., 2002). Direct lights are usually not isotropic due to light characteristics. For example, street light lamps might be top-covered. Therefore the lamps could not be viewed from a nadir look but may be observed from off-nadir measurements (and in all cases produce reflected light off the surface). Building lights consist of indoor lights through windows, direct lights installed on building façade, and building reflected lights common over commercial buildings (Li et al., 2020). Most building lights might only be observed from an off-nadir view. Studies have found that nighttime light radiance illustrates a strong non-linear relationship with VZA fitted by the quadratic model (Li et al., 2019; Tong et al., 2020). NTL radiance usually increases toward high VZA at suburban residential regions while revealing a decreasing trend across dense urban centers. View Azimuth Angle (VAA) effect was weak with minor improvement for the model

Table 1

Locations of chosen artificial light sites. The metrics (Section 2.3) were calculated based on the mean value of 3 by 3 pixels in 2018 from daily VNP46A2 product. Red colour of $-b/2a$ indicated negative a value.

Site	Location	Latitude	Longitude	Land use type	CV	SD	$NDHD_{NTL}$	-b/(2a)	Coefficient of determination (R-squared) before/after
site1	Los Angeles	34.05	-118.26	commercial area	0.26	54.21	0.42	46.82	0.00/0.00
site2	Los Angeles	34.01	-118.31	residential area	0.15	6.21	0.29	13.19	0.04/0.00
site3	Riverdale	36.43	-119.86	rural	0.23	2.69	0.27	15.60	0.19/0.02
site4	New York	40.76	-73.98	commercial area	0.31	83.60	0.75	44.51	0.00/0.01
site5	New York	40.70	-73.51	residential area	0.36	9.81	0.18	10.31	0.04/0.03
site6	Greenwich	41.07	-73.61	Residential area	0.41	1.57	0.17	30.38	0.19/0.00
site7	West Milford	41.03	-74.39	rural	0.51	0.79	0.45	7.54	0.24/0.00
site8	Sydney	-33.87	151.21	commercial area	0.21	28.21	0.3	52.86	0.00/0.01
site9	Sydney	-33.89	151.10	residential area	0.15	2.20	0.19	-40.34	0.18/0.01
site10	Oberon	-33.70	149.86	rural	0.42	2.92	0.1	39.82	0.20/0.02
site11	Beijing	39.93	116.40	commercial area	0.15	5.90	0.06	26.14	0.04/0.00
site12	Beijing	39.91	116.45	commercial area	0.25	21.74	0.15	47.26	0.01/0.00
site13	Beijing	39.85	116.41	residential area	0.18	7.40	0.04	30.65	0.03/0.00
site14	Bianjiapucun	38.81	116.22	rural	0.36	0.31	0.22	-13.40	0.40/0.04
site15	Dubai	25.08	55.14	commercial area	0.18	47.31	0.52	40.24	0.00/0.00
site16	Dubai	25.17	55.22	residential area	0.12	9.25	0.05	31.51	0.03/0.01
site17	Sharjah	25.21	55.73	rural	0.3	2.15	0.06	57.70	0.32/0.01
site18	Jerusalem	31.76	35.21	commercial area	0.11	10.94	0.07	34.71	0.02/0.00
site19	Jericho	31.86	35.46	Residential area	0.19	6.35	0.11	19.41	0.04/0.01
site20	Na'omi	31.91	35.47	rural	0.33	2.52	0.09	4.27	0.34/0.02
site21	Rome	41.90	12.48	commercial area	0.18	39.32	0.47	44.18	0.00/0.00
site22	Rome	41.88	12.57	residential area	0.13	6.11	0.07	30.14	0.02/0.00
site23	Rome	41.86	12.68	residential area	0.14	5.08	0.06	-12.51	0.02/0.00
site24	Moricone	42.12	12.77	rural	0.32	2.89	0.25	14.29	0.12/0.01

fitting (Li et al., 2019). At an urban commercial center formed by tall buildings, nadir looks observe more light from surface reflected street light, vehicle-emitted light, and commercial shop stores located at the buildings' ground floor. Tall buildings are more likely to shield lights along roadways. Therefore off-nadir observations sense more light from direct lights installed on building façade, building reflected lights, and indoor lights through windows.

3.1.1. *Zenith angle*

NTL radiance at commercial centers dominated by tall buildings such

Table 2

Location of the 37 AERONET sites and the metrics of AOD in 2019. 'Nstd' is the nighttime 500 nm AOD standard deviation. 'Nmean' corresponds to the mean nighttime AOD. 'StdDif' is the standard deviation of the difference between daytime and nighttime AOD. 'MeanDif' is the mean difference between daytime and nighttime AOD.

Site name	Latitude	Longitude	Land type	Nstd	Nmean	StdDif	MeanDif
Bandung	−6.89	107.61	big city	0.32	0.63	0.32	0.29
Beijing-CAMS	39.93	116.32	bit city	0.42	0.48	0.29	0.23
Chiba_University	35.63	140.10	big city	0.22	0.2	0.13	0.1
Dhaka_University	23.73	90.40	big city	0.38	0.85	0.25	0.3
Fukuoka	33.52	130.48	big city	0.21	0.23	0.08	0.08
CCNY	40.82	−73.95	big city	0.1	0.14	0.06	0.06
NASA_Ames	37.42	−122.06	big city	0.02	0.08	0.02	0.02
MD_Science_Center	39.28	−76.61	city	0.02	0.11	0	0
Mongu_Inn	−15.27	23.13	city	0.08	0.17	0.04	0.04
Kanpur	26.51	80.23	city	0.39	0.59	0.33	0.25
Burjassot	39.51	−0.42	city	0.09	0.12	0.04	0.04
Medellin	6.26	−75.58	middle town	0.04	0.13	0.03	0.04
Palangkaraya	−2.23	113.95	middle town	0.81	0.64	0.43	0.26
Reykjavik	64.13	−21.90	middle town	0.08	0.15	0.04	0.04
Bac_Lieu	9.28	105.73	small town	0.16	0.36	0.14	0.15
Dalanzadgad	43.58	104.42	small town	0.09	0.11	0.07	0.04
Fresno_2	36.79	−119.77	small town	0.04	0.11	0.02	0.03
GSFC	38.99	−76.84	small town	0.09	0.13	0.05	0.05
Jambi	−1.63	103.64	small town	0.82	0.77	0.62	0.38
Payerne	46.81	6.94	small town	0.07	0.15	0.05	0.06
Raciborz	50.08	18.19	small town	0.14	0.21	0.07	0.08
SDSU_IPLab	44.32	−96.79	small town	0.08	0.15	0.06	0.06
Thimphu	27.47	89.64	small town	0.15	0.27	0.1	0.13
Gangneung_WNU	37.77	128.87	city edge	0.12	0.2	0.2	0.14
Kashi	39.50	75.93	middle town edge natural	0.23	0.5	0.14	0.17
Caillouel_COBIACC	49.62	3.13	rural/village	0.07	0.16	0.03	0.03
Ilorin	8.48	4.68	village	0.47	0.72	0.22	0.18
Migal	33.24	35.58	village	0.13	0.26	0.1	0.1
Amazon_ATTO_Tower	−2.14	−59.00	natural area	0.08	0.14	0.02	0.02
Barrow	71.31	−156.67	natural area	0.01	0.07	0.01	0.01
DEWA_ResearchCentre	24.77	55.37	natural area	0.19	0.39	0.09	0.1
Huancayo-IGP	−12.04	−75.32	natural area	0.09	0.12	0.04	0.03
Kangerlussuaq	67.00	−50.62	natural area	0.11	0.14	0.11	0.06
Lulin	23.47	120.87	natural area	0.08	0.07	0.04	0.04
Railroad_Valley2	38.50	−115.69	natural area	0.04	0.07	0.03	0.02
SERC	38.89	−76.56	natural area	0.11	0.15	0.06	0.06
Upington	−28.38	21.16	natural/desert	0.08	0.1	0.04	0.03

as Site-1 in Fig. 2, decreased toward high VZA,looking at an oblique angle toward the lights. Site-18 is located at an urban center with mixed land-use types and dominated by four to six-story buildings. The radiance first decreased and then slightly increased toward high VZA. The relationship is sophisticated over residential sites. Site-2, residential areas dominated by single-story houses, showed an increasing trend with VZA. The relationship at Site-13 was nearly neutral, and the radiance of Site-22 slightly decreased toward high VZA. Site-13 is comprised of tall apartments with most buildings higher than nine-story while Site-22 is formed by approximate five-story apartments. Site-3 is located in a rural area dominated by single-family houses and surrounded by farmland. The radiance of this site continuously increased along with VZA.

The variation of NTL radiance with VZA of the 24 sites in 2018 was quantified by CV, $\text{NDHD}_{\text{NTL},}$ and darkspot/hotspot location indicated by $-b/(2a)$ from quadratic model fitting (Table 1). Rural sites had the highest CV values with a large standard deviation than mean values (e.g., Fig. 16 Site- 6) though the SD values are the least. CV of most commercial center locations was slightly higher than the adjacent residential regions. The variation of commercial centers appears to be dominated by observations around nadir look observations (e.g. Fig. 19 Site-21). Commercial center sites had the largest NDHD_{NTL} as a result of high NTL radiance at nadir look (hotspot) and dramatically dropped radiance toward high VZA (darkspot). The NTL radiance of rural Site-3, 7, 14, and 24 illustrated an increasing trend toward high VZA with NDHD_{NTL} values above 0.2. Near zero NDHD_{NTL} indicated low or no relationship between NTL radiance and VZA such as several rural sites (Site-13, 17, and 20), residential sites (Site-16, 18, 22, and 23), and commercial center sites with low height buildings (Site-11 and 18). $-b/(2a)$ was utilized to locate the cold effect of radiance (Li et al., 2019). The $-b/(2a)$ value is usually high over commercial sites where NTL radiance goes down with VZA and low at sites that NTL radiance elevates with VZA. The effect of $-b/(2a)$ depends on the coefficient a which indicates the curvature of the quadratic model. The coefficient a value is relatively low, closing to zero in particular at sites unrelated to VZA. Site-10 and 22 had a negative coefficient a values. NTL radiance of these two sites was relatively stable over near nadir looks and slightly decreased toward high VZA, therefore here $-b/(2a)$ indicated hotspot instead of darkspot VZA (e.g. Fig. 2, Site-22). Site-22 and 23 are both located at the metropolitan of Rome and dominated by four-six story apartments. The radiance of Site-22 decreased toward high VZA while Site-23 showed an opposite trend.

The data acquisition time is the same for nadir looks while apart from approximate 2 h at VZA above 60 degrees at mid/low latitude areas (Fig. 2). This indicated that high radiance variation at commercial centers over nadir is not impacted by the diurnal changes (Li et al., 2020). The high variation at nadir is also less influenced by VAA since nadir looks mainly observe lights from the surface and almost no lights from the side of the buildings. Since the vegetation effect over commercial centers is also small (Fig. 16), the high variation could be caused by i) human activities and changes that are common across dense commercial centers (e.g., holiday lighting), ii) incorrect AOD used for NTL radiance retrieval (Fig. 13), or iii) cloud/snow contamination.

NTL radiance of most sites was normally distributed while several sites (e.g. Site-4, 6, 15, and 17) showed skewed distribution which is highly related to VZA (Fig. 3). NTL radiance of most observations was low at rural Site-6 and 17. The radiance of only a few observations was extremely high to nearly 1000 $\text{nWcm}^{-2}\ \text{sr}^{-1}$ around nadir looks at commercial sites (e.g., Site-4 and 15).

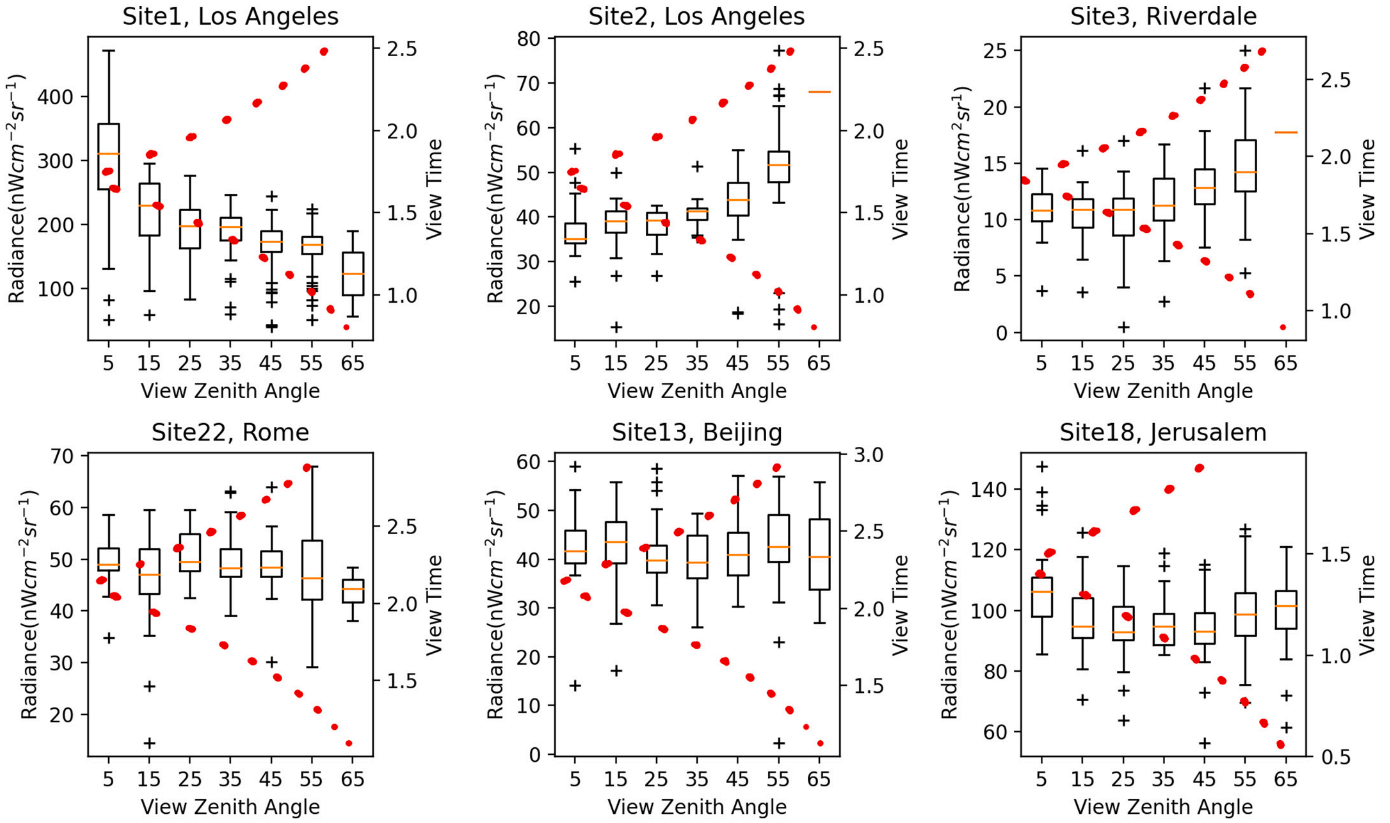

Fig. 2. Boxplot of NTL radiance along with VZA in 2018. Acquisition time was plotted as red dots. The location of each site was listed in Table 1. VZA was grouped to seven bins (0–10, 10–20, 20–30, 30–40, 40–50, 50–60, and 60–70 degrees). (For interpretation of the references to colour in this figure legend, the reader is referred to the web version of this article.)

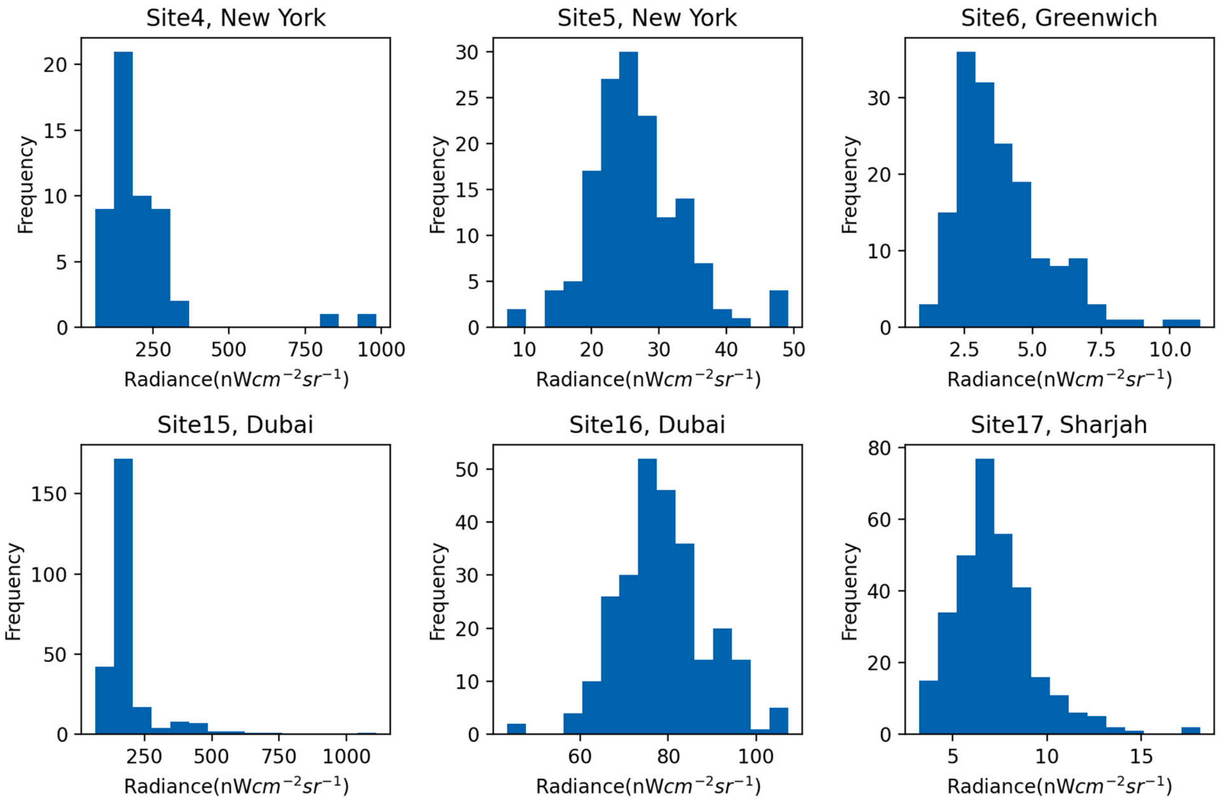

Fig. 3. Histogram of NTL radiance at Site-4, 5, 6, 15, 16, and 17.

3.1.2. View Azimuth Angle (VAA)

Nighttime light pollution is originated from sky luminance from atmospheric scattered artificial light (Falchi et al., 2016). Although the VAA, relative to north, effect is less significant than the VZA effect (Li et al., 2019), the impact of VAA on NTL radiance was found at urban edge region driven by diffuse atmospheric scattering along the satellite scan direction (Sanchez de Miguel et al., 2020; Tong et al., 2020) (Figs. 4 and 5). Atmospheric scattered urban artificial light increased the NTL radiance over natural 'no-NTL' areas, particularly if the target was observed from the along-scan direction passing through the sky above the urban zone (Fig. 4). Elevated radiances over natural areas were consistent with VAA at Las Vegas during moon free night (Fig. 5). For example, NTL radiance of natural area was enhanced to 3.0 nWcm^{-2} sr^{-1} at Las Vegas on Day of Year (DOY) 343, 2018. This effect is comparable to NTL radiance from villages. This scenario also indicated that the radiance of darker areas within urban corridors could be increased by adjacent brighter urban centers by VAA effects.

3.1.3. Building structure

NTL radiances at commercial sites with tall buildings were mostly higher than 100 nWcm^{-2} sr^{-1} particularly for nadir looks (e.g. Fig. 2 Site-1, Fig. 3 Site-4, 15), and brighter than the sites with low buildings. For instance, the median radiance of Beijing's old town area (Site-11) with low buildings was 39 nWcm^{-2} sr^{-1} in 2018, much lower than the median radiance of nearby Site-12 (87 nWcm^{-2} sr^{-1}) dominated by high rise buildings. NTL radiance was also positively associated with building heights with R^2 of 0.388 in Los Angeles, but the relationship was weak over tall buildings (Fig. 6 (c)). The R^2 between building heights and NTL radiance has no significant relationship with VZA and VAA in Los Angeles based on 181 days of mostly clear daily VNP46A2 data in 2012. The NTL radiance of commercial urban centers mainly comes from the traffic, billboard signs, and floodlights and generally higher than the radiance of other land uses. The NTL radiance emitted from the windows from off-nadir measurements of Los Angeles urban center is also much higher than other regions. The R^2 is not high since the NTL radiance could be high at low building height area. For example, the NTL radiance at Port of Long Beach with nearly no buildings, southwest of Los Angeles, is close to Los Angeles commercial urban center. Tall buildings used for business activities have more lights emitted from street-level sources, building façades, and window lights around midnight. The radiance of high-rise residential apartments are also darker than commercial buildings though with similar height. Reflected street and building façade lights of residential apartments are much lower than commercial buildings. For instance, the radiance of commercial center Site-21 with low height buildings was much higher than the residential area with similar building heights. Therefore, considering land-use types and changes is a key prerequisite for characterizing the relationship between building heights and NTL radiance.

Our results suggest that building height is one of the key factors driving the angular effect in NTL radiance (Li et al., 2019). NTL radiance from nadir look is mainly from street lights with less contribution from building façade and window lights. Off-nadir observations over tall building areas are dominated by reflected lights from building façade and direct lights from side windows while the street lights are shielded by tall buildings. The magnitude of lights from the building façade is related to building type (e.g., commercial or residential). The building side facing to commercial streets is usually brighter than other sides, which could induce VAA related NTL radiance variation.

3.2. Surface BRDF/albedo

High surface BRDF/albedo increases reflected lights from street lamps and lunar irradiance (Román et al., 2018). The atmospheric effect is also enhanced by a high surface BRDF/albedo area with elevated multi-scattering (Section 3.4). The albedo of the areas with NTL radiance larger than 2.0 nWcm^{-2} sr^{-1} was mainly less than 0.45, and the peak albedo was around 0.1–0.15 (Fig. 7). The albedo on DOY 180 was slightly higher than the values on DOY 360 in 2012. Most artificial lights are distributed in the northern hemisphere where vegetation is at growing peak condition in the late spring (DOY ~180). Vegetation reflectance at DNB (500–900 nm) is also higher than most urban infrastructure properties (Moreira and Galvão, 2010; Yan et al., 2015).

The magnitude of surface NTL radiance increased by moonlit is comparable to artificial light radiance in rural and suburban regions (Fig. 8). As such, reflected moonlight radiance varying with the lunar cycle is another major source of noise for time series analysis, particularly for short-term events such as power outage recovery (Román et al., 2019). The recovery could be false caused by the moon phase changing from new moon to full moon.

Reflected lunar radiance also rises with higher albedo and downward lunar irradiance (Fig. 9). To illustrate, we calculated the reflected lunar radiance with AOD set to 0.05 by the radiative transfer atmospheric correction model (Román et al., 2018) to minimize the atmospheric effect. Note the reflected lunar radiance is positively linear associated with albedo. Lunar irradiance was approximately 140 nWcm^{-2} during the Full Moon. Reflected lunar radiance was about 5 nWcm^{-2} sr^{-1} at surface albedo peak value of 0.15 over artificial light regions (Fig. 7) and reached to above 25 nWcm^{-2} sr^{-1} when albedo is 0.9 for snow or cloud

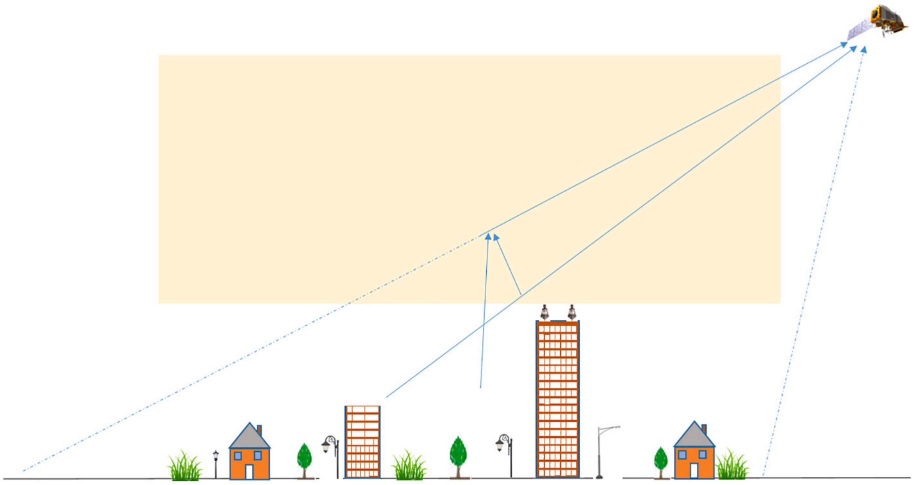

Fig. 4. A schematic diagram describing the increased in NTL radiance over a natural area adjacent to urban corridors due to atmospheric scattering effect (path radiance) along the satellite scan direction.

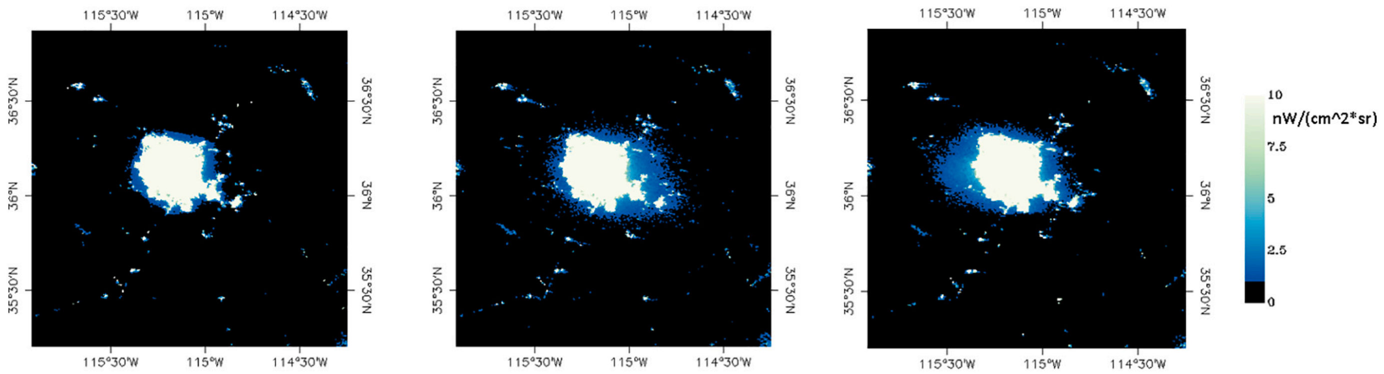

DOY 111, 2018, VZA=10 degree VAA = -76 degree

DOY 13, 2018, VZA = 55 degree VAA = -72 degree

DOY 343, 2018, VZA = 56 degree VAA = 94 degree

Fig. 5. VNP46A1 NTL radiance at Las Vegas viewed from (a) nadir look on DOY 111, 2018, (b) large VZA with satellite located at the left side of Las Vegas on DOY 13, 2018, and (c) large VZA with satellite located at the right side of Las Vegas on DOY 343, 2018.

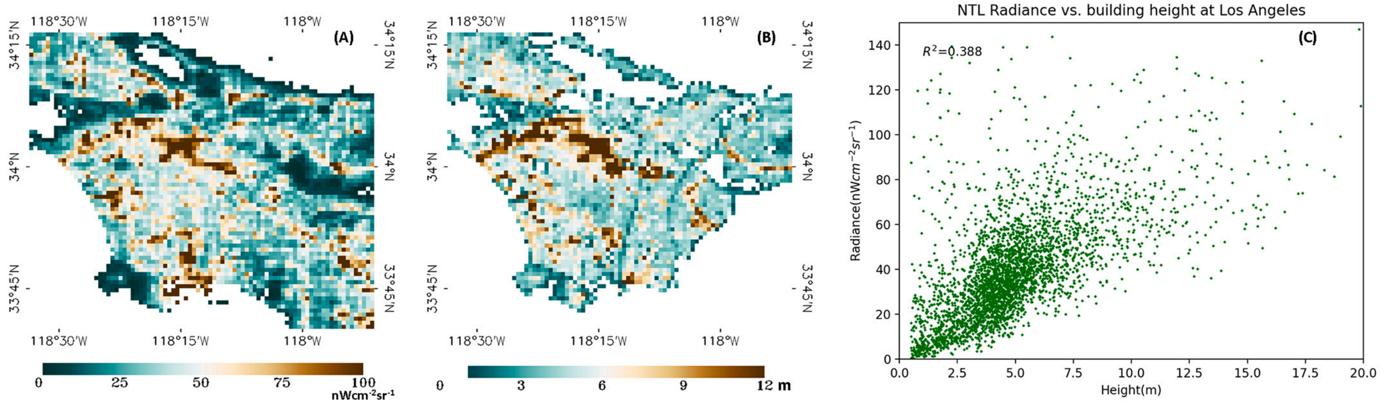

Fig. 6. Relationship (c) of annual composite VIIRS Nighttime Light (500 m) in 2012 (a) and building heights (LARIAC4) generated from imageries including 2012 and 2013 (b) at Los Angeles.

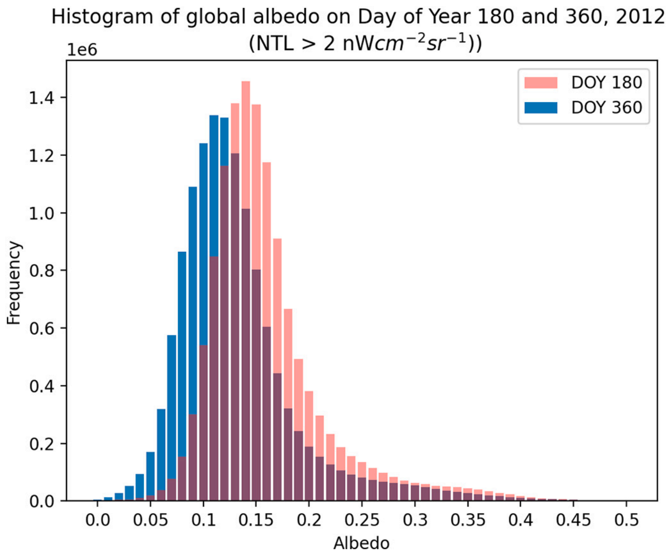

Fig. 7. Histogram of surface snow-free DNB albedo over global areas with NTL radiance larger than 2nWcm^{-2} sr^{-1} on DOY 180 and 360 in 2012.

on Full Moon nights.

3.3. Lunar effect correction

For NASA's Black Marble product, reflected lunar radiation is routinely corrected based on surface BRDF/albedo and lunar irradiance (Fig. 10). A radiometry-based lunar irradiance model (MT2009) (Miller and Turner, 2009) calculates lunar irradiance. MT2009 provides 1 nm spectral resolution lunar irradiance and aims to generate TOA downwelling lunar irradiance at any location/time. Lunar phase angle, lunar spectral albedo, and Sun/Moon/Earth geometry are crucial parameters in the model while the opposition effect, libration effect, and waxing and waning lunar phases are currently ignored in the initial MT2009 model. The spectral lunar irradiance result is convolved with the VIIRS DNB's post-launch spectral response function to yield downwelling TOA lunar irradiance for a given scene. The uncertainty of MT2009 due to approximations mentioned above was estimated on the order of 7–12% (Miller and Turner, 2009), with the majority of uncertainty arising from the lunar phase and opposition being the largest contributors. Improvements to this model to account for these effects are forthcoming, are anticipated to further reduce uncertainty to ~5%. Modeled lunar radiance matched DNB observations with R^2 of 0.989 evaluated at Dome C Antarctic and Greenland (Shao et al., 2014, 2013). MT2009 underestimated the lunar irradiance near the full moon by ~7% (Cao et al., 2019; Zeng et al., 2018). Zeng et al. (2018) also improved the MT2009 on waxing and waning lunar phases based on SeaWiFS lunar observations. The uncertainty of lunar irradiance estimation by topography and

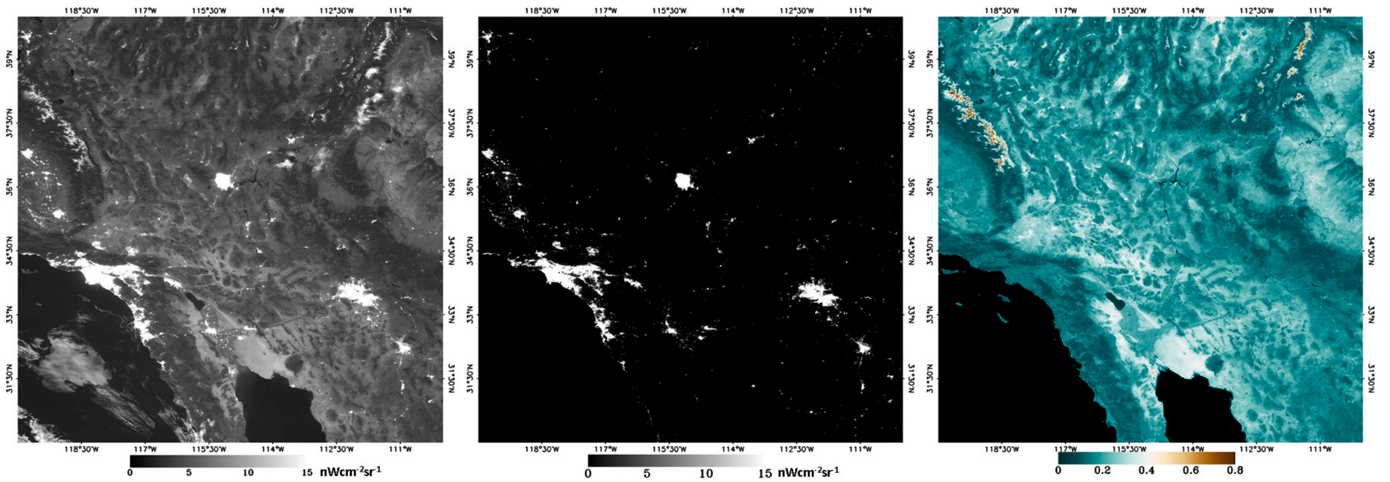

Fig. 8. VNP46A1 TOA radiance (left), VNP46A2 lunar BRDF-corrected radiance (middle), and DNB albedo (right) at tile h06v05 on a Full Moon night from DOY 116 in 2013.

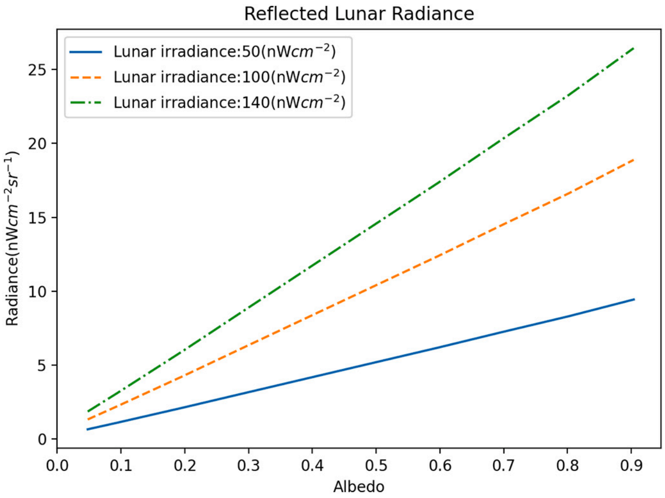

Fig. 9. Reflected lunar radiance along with albedo and lunar irradiance.

libration effects is very small, and lunar surface heterogeneity influence is low at coarser resolution (Zeng and Li, 2019).

We illustrate how lunar reflected radiance is successfully removed in Black Marble (VNP46) standard processing, both over natural (Román et al., 2018) and artificial light areas (Fig. 10). The R^2 between lunar BRDF-corrected radiance and moon illumination fraction dropped to less than 0.044 at all of the four sites in Fig. 10. Lunar contribution increases when the moon illuminated fraction is larger than 40% and grows rapidly beyond moon illuminated fractions of 80%. The influence of lunar radiance highly depends on surface BRDF/albedo (Fig. 9) and is much larger over rural areas than urban centers (Fig. 10). As such, methods that do not consider these higher-order effects will likely suffer from additional retrieval uncertainties.

NTL TOA radiance increased from ~1 $nWcm^{-2}\ sr^{-1}$ during moon-free night to 10.0 $nWcm^{-2}\ sr^{-1}$ during full moon night at rural Site-1. The R^2 of linear regression was 0.401 between moon illumination fraction and TOA radiance at Site-1. TOA NTL radiance was doubled from moon free to full moon nights at Site-9 and Site-10 with R^2 reduced to 0.178 and 0.203, respectively. Urban center regions were less impacted by lunar irradiance with nearly zero R^2 between moon illumination fraction and TOA NTL radiance at Site-8.

3.4. Atmospheric effect

Atmosphere particles scatter light and thus reduce observed upwelling urban artificial light radiance (Fig. 13). The nighttime atmosphere can also enhance the radiance of natural areas in close proximity to urban corridors (Fig. 5) (Sanchez de Miguel et al., 2020; Tong et al., 2020). Daytime AOD from the previous day is utilized for Black Marble product atmospheric correction as no nighttime AOD product is currently available. A nighttime radiative transfer model was developed to retrieve nighttime AOD using the blurring effect of aerosol layers on an artificial light source (Johnson et al., 2013; McHardy et al., 2015; Zhang et al., 2019, 2008) and indicated that the diffuse correction is important for heavy aerosol loadings (Zhang et al., 2019). Wang et al. (2020b)) developed a nighttime shortwave 1D UNified and Linearized Radiative Transfer Model (UNL-VRTM) to simulate the TOA radiance and address the questions associated with aerosol. The results illustrated that the VIIRS DNB's Relative Spectral Response (RSR) Function and surface illumination source spectrum are crucial factors to reduce the uncertainty of AOD retrieval.

The difference between daytime and nighttime 500 nm AOD of the chosen 37 AERONET sites was relatively small and less than 0.05, 0.1, and 0.25 for 58%, 73%, and 92% of the observations respectively in 2019 (Fig. 11 (a)). 62% of nighttime AOD was less than 0.2 (Fig. 11 (b)). Several sites experienced strong seasonal variation (e.g., Huancayo, Dalanzadgad, Arm_SG, GSFC, Rexburg) with higher AOD during summer (Fig. 12). While the seasonal pattern of the difference of daytime and nighttime AOD is minor. Mostly the daytime and nighttime AOD difference is less than 0.1 (Figs. 11 and 12). The effect of 0.1 different AOD on NTL radiance is less than 5% (Fig. 13) which usually has much lower effect than vegetation (e.g. Fig. 16 Site-6). Six sites of the difference between daytime and nighttime AOD showed seasonal patterns. Four of them (Burjassot, CCNY, Chiba_University, and GSFC) have artificial light and the remaining two sites (DEWA_ResearchCentre and SERC) are located in natural areas. The daytime and nighttime AOD difference of sites Burjassot, CCNY, and Chiba_University showed normal distribution centered at zero. Only GSFC site showed few more days with daytime AOD higher than nighttime AOD during summer. AOD was also relatively higher over urban areas than natural and suburban locations (Table 2). High AOD over urban areas could be caused by human activities and related fossil fuel emissions. Most of the big cities experienced high AOD mean (up to 0.85) and standard deviation (up to 0.42) (Fig. 12 and Table 2). The mean difference and standard deviation AOD between daytime and nighttime of big city sites were large which reached up to 0.30 and 0.32 respectively. The high difference between daytime and nighttime AOD significantly increases the uncertainty

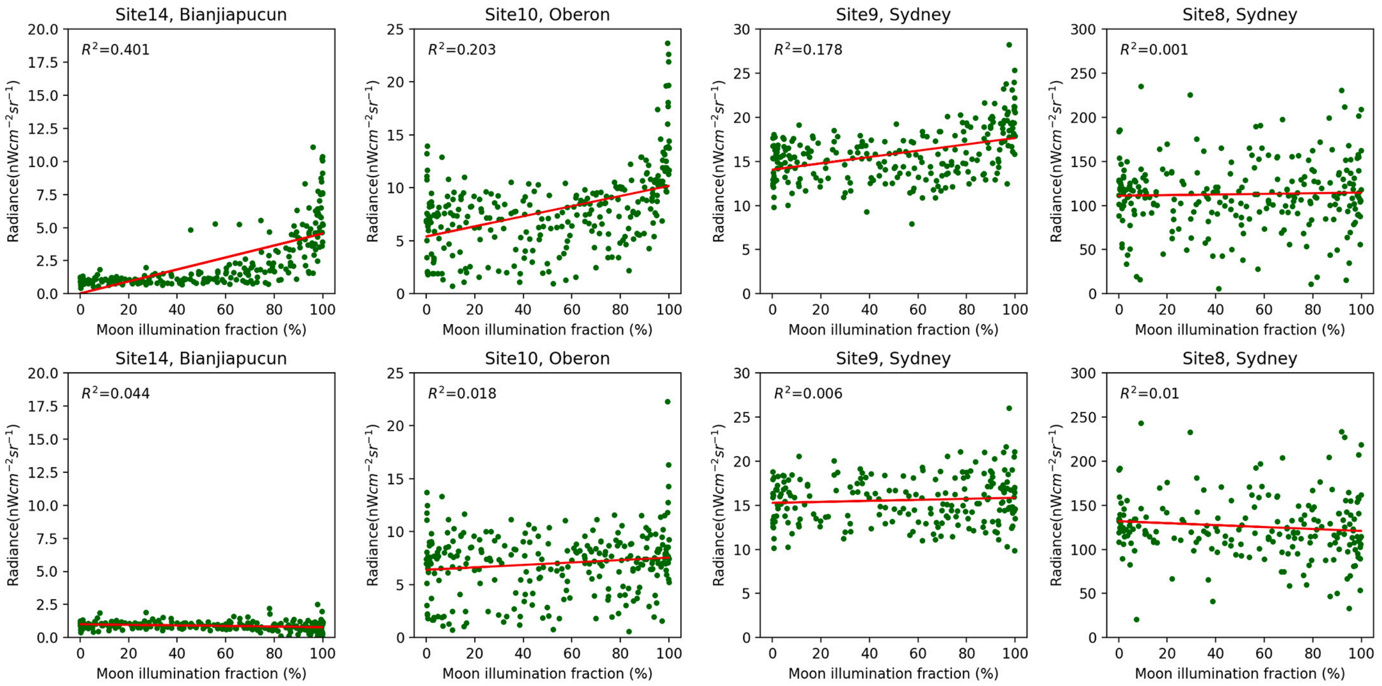

Fig. 10. Relationship between moon illumination fraction and TOA NTL radiance (top) and lunar BRDF-corrected radiance (bottom) at Site-4, 10, 9, and 8 in 2018.

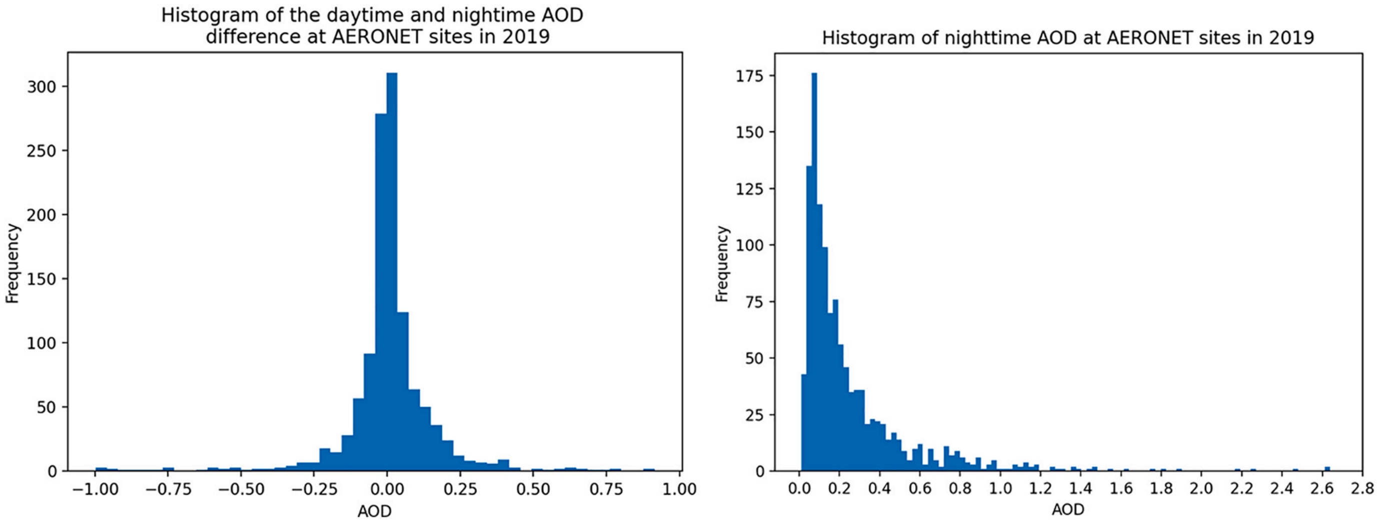

Fig. 11. Histogram of the difference of daytime and nighttime AOD (left) and histogram of nighttime AOD (right) over the 37 AERONET sites listed in Table 2 in 2019.

during NTL atmospheric correction.

We estimated the relative change of radiance (Eq. (2)) using the Black Marble atmospheric correction radiative transfer model during the moon-free night, excluding lunar effect (Fig. 13). The relative change of radiance has no relationship with the magnitude of surface NTL radiance during moon-free nights. TOA NTL radiance was reduced with higher AOD loadings. High surface albedo mitigated the AOD effect with more downward atmosphere scattered light reflected back to the sky. AOD effect was enhanced with the increase of VZA, which raised the length of light interacting with the atmosphere. NTL radiance decreased over 30% with 0.8 AOD, 0.05 surface albedo, and 60-degree VZA. The relative change was −12% for typical retrieval conditions with a surface albedo of 0.1 and AOD of 0.2.

California experienced severe wildfires in 2020. Fresno was covered by fire smoke in mid-Aug and Sep. Fig. 14 illustrated that TOA NTL radiances at cloud-free nights with heavy AOD loadings (AOD at 500 nm > 1.0) were dimmer than regular days in particular during the days with high VZA with longer path length through heavy AOD atmosphere. These results underscore the critical need for consideration of atmospheric conditions in the retrieval of NTL time series. The use of TOA NTL composites should thus be avoided, particularly for studies requiring a consistent NTL time series record to assess human activities and changes.

3.5. Cloud mask

NASA VNP35 nighttime cloud mask is currently derived from the VIIRS thermal infrared bands (Hutchison et al., 2005). VNP35 algorithm tuned the thresholds to balance the leakage and false alarms though shared the same core algorithm with MODIS cloud mask product

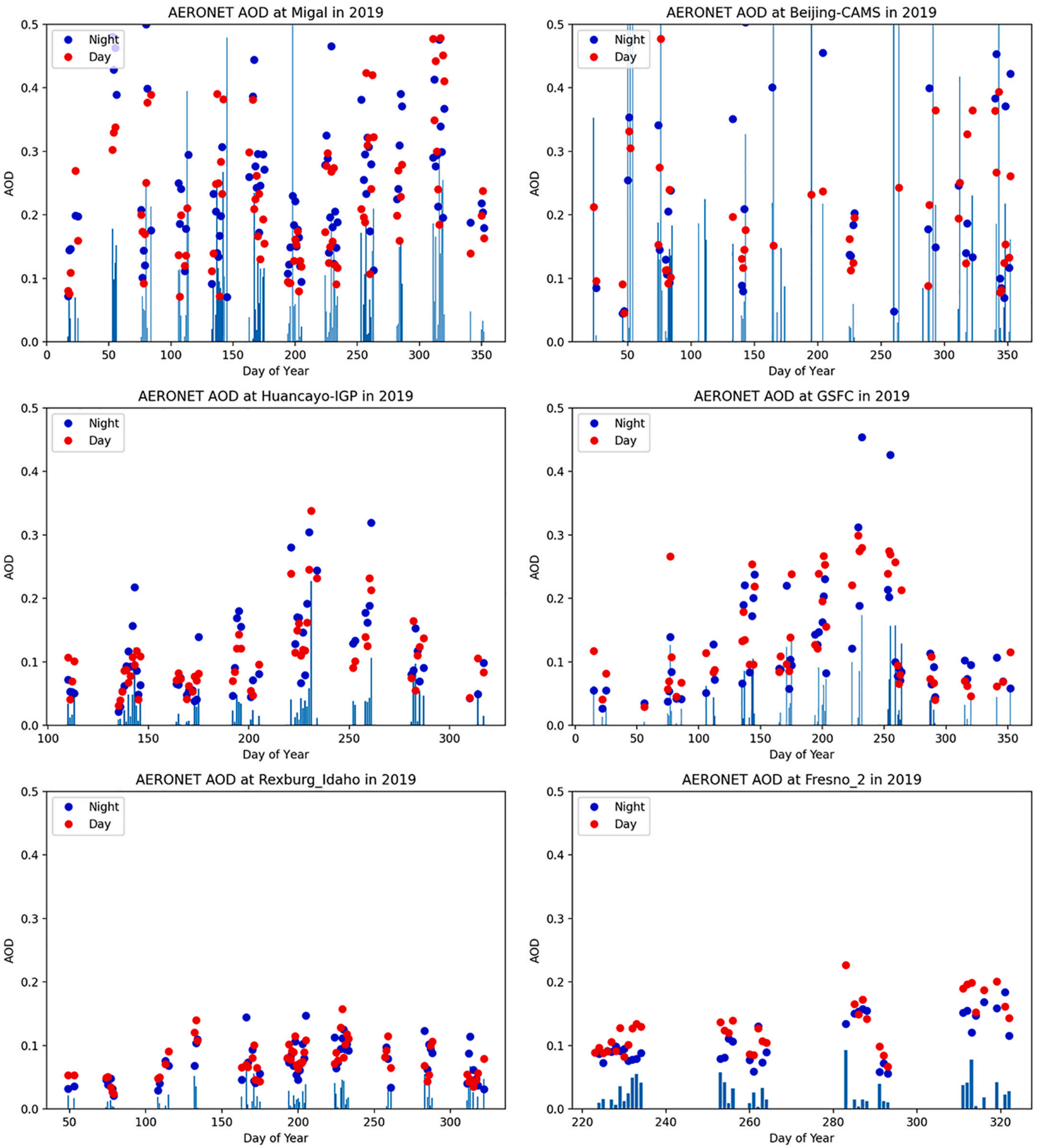

Fig. 12. Temporal daytime and nighttime AOD over AERONET sites in 2019. The dates with AOD were clustered since AOD was measured during moonlit nights. The vertical bar represents the difference AOD between daytime and nighttime.

(MOD35) (Ackerman et al., 1998). The hit rate of nighttime VNP35 cloud mask was 86.4%, 94.5%, and 94.0% for global, 60s-60N land, and desert, respectively, evaluated using Cloud-Aerosol Lidar with Orthogonal Polarization (CALIOP) product (Kopp et al., 2014). The false alarm was 4.4%, 1.5%, and 0.9% while the missed cloud was 7.3%, 3.7%, and 4.9% respectively. Poor accuracy was found over the polar region (Kopp et al., 2014). A random forest method was developed using DNB only to detect clouds with the accuracy of up to 85% for urban test sites (Joachim and Storch, 2020). Urban regions usually suffer from the heat islands effect making it difficult to tune the thresholds for cloud detection. Note, for example, some cloud coverage over urban regions in tile h29v05 on DOY 004, 2016 (e.g. Fig. 15 (d) black rectangle region) was not detected. Nighttime thin cirrus cloud detection is challenging since the signal of shortwave-infrared 1.38 μm band, usually utilized to detect

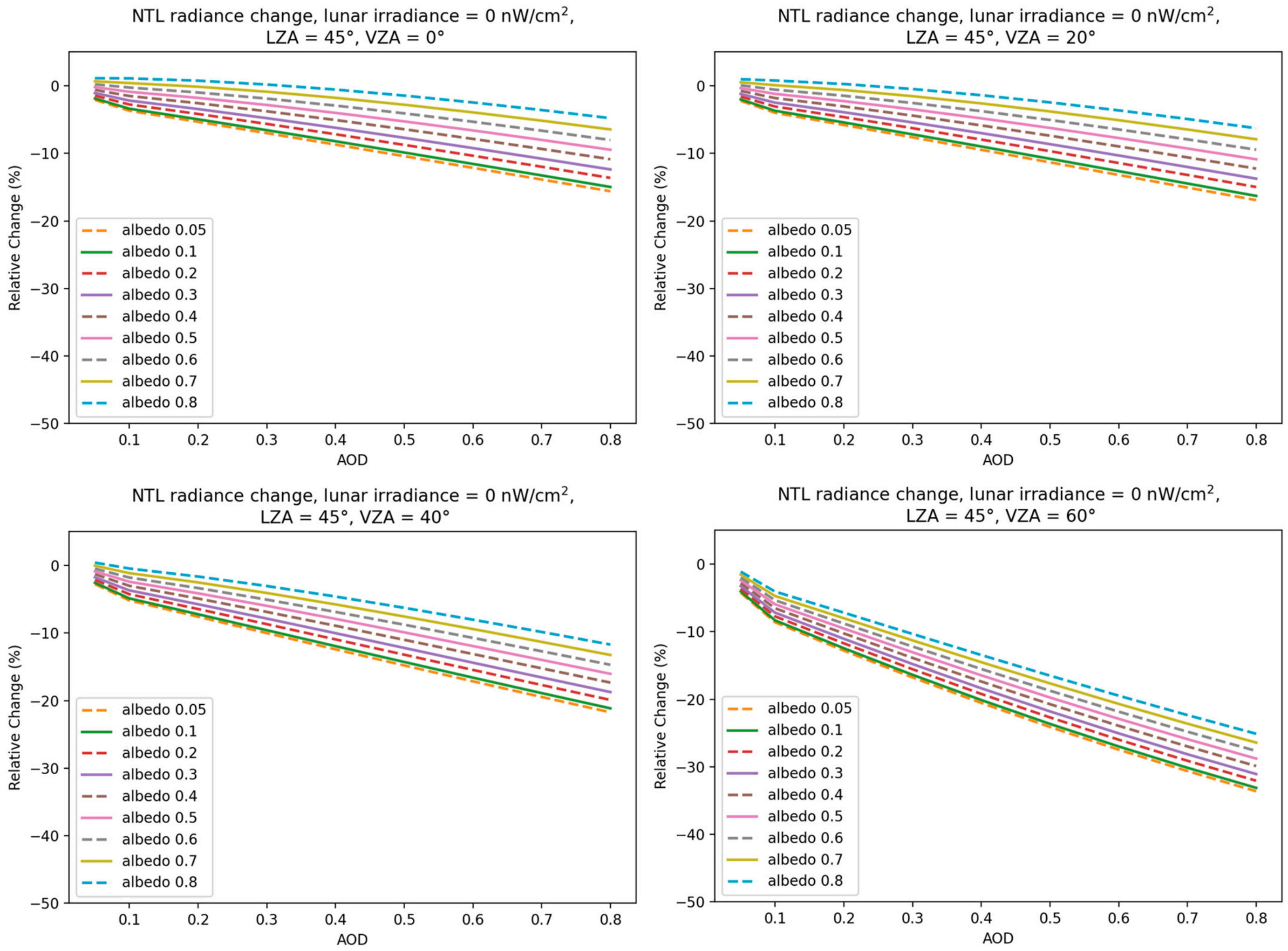

Fig. 13. Relative change of NTL radiance along with AOD and albedo over different view angles.

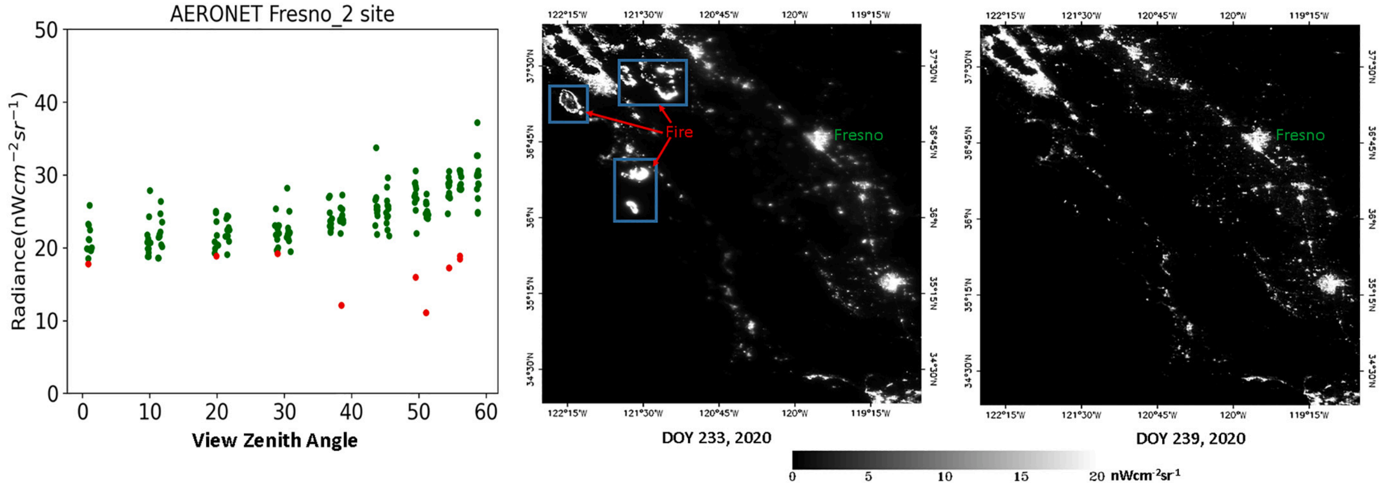

Fig. 14. DNB TOA NTL radiance with VZA at AERONET Fresno site in 2020 (left). Red dots represent NTL radiance corresponding to nights with heavy aerosol loadings caused by California wildfires (nighttime AOD at 500 nm > 1.0). DNB TOA NTL radiance on DOY 233 (middle, during wildfire) and 239 (right, after wildfire) in 2020. (For interpretation of the references to colour in this figure legend, the reader is referred to the web version of this article.)

cirrus cloud (Ackerman et al., 1998; Gao and Kaufman, 1995; Hutchison et al., 2012; Zhu et al., 2015), is weak at night. Cirrus cloud contamination is also important for nighttime aerosol retrieval (Johnson et al., 2013).

Cloud misclassification is one of the major sources of NTL radiance outliers which differ significantly from other observations. Cloud impacts on artificial light also depend on cloud types and moon conditions (Garstang, 2007; Jechow et al., 2019). Partial artificial lights could

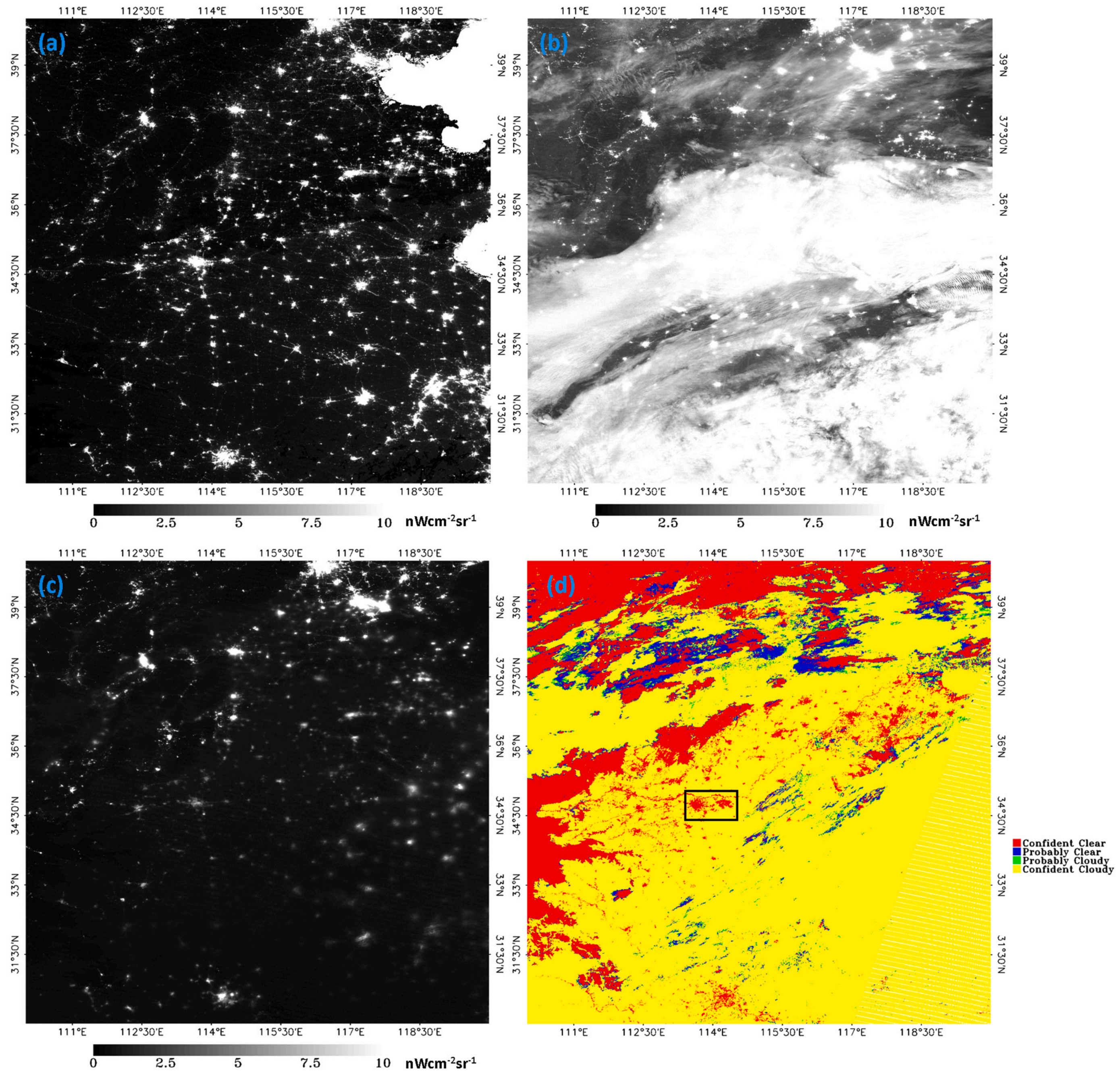

Fig. 15. Impact of cloud contamination for tile h29v05. (a) gap-filled surface NTL radiance on DOY 027 in 2016, (b) TOA radiance during the moonlit night on DOY 027 in 2016, (c) TOA radiance during the moon-free night on DOY 004 in 2016, and (d) VNP35 cloud mask on DOY 004 in 2016.

penetrate thin clouds, while thick clouds can completely obscure upwelling lights. Thin clouds can reduce the artificial light radiance (e.g. Fig. 15 (c) east part of the tile), and can result in a drop in NTL radiance to near-zero when covered by thick cloud (Fig. 15 (c) south part of the tile) on moon-free nights.

Cloud contamination is also complicated on moonlit nights. NTL radiance over natural areas increases from zero to cloud reflected lunar radiance. The observed radiance over rural areas increases if artificial light radiance is lower than cloud reflected lunar radiance, decreasing when upwelling artificial light radiance is higher than cloud reflected lunar radiance covered by thick clouds. The radiance changes in rural areas covered by thin clouds depend on the sum of reduced radiance and cloud-reflected lunar radiance. Both thin and thick clouds reduce the NTL radiance over the urban centers since the cloud reflected lunar radiance is much lower than artificial light. Cloud reflectance could reach 0.9 over the DNB spectrum (Schlundt et al., 2011). Cloud reflected lunar radiance can be larger than 25 nWcm^{-2} sr^{-1} for thick clouds during full moon night (Fig. 9), assuming no aerosol loading above the cloud.

3.6. Vegetation effect

Vegetation phenology is one of the drivers of NTL seasonal variation (Levin, 2017; Levin et al., 2020; Román et al., 2018). For regions characterized by deciduous trees, vegetation canopy leaves block artificial lights during the leaf-on season while more light could penetrate the vertical layer because of the larger gap fraction during the leaf-off period. Various algorithms have been applied to eliminate the

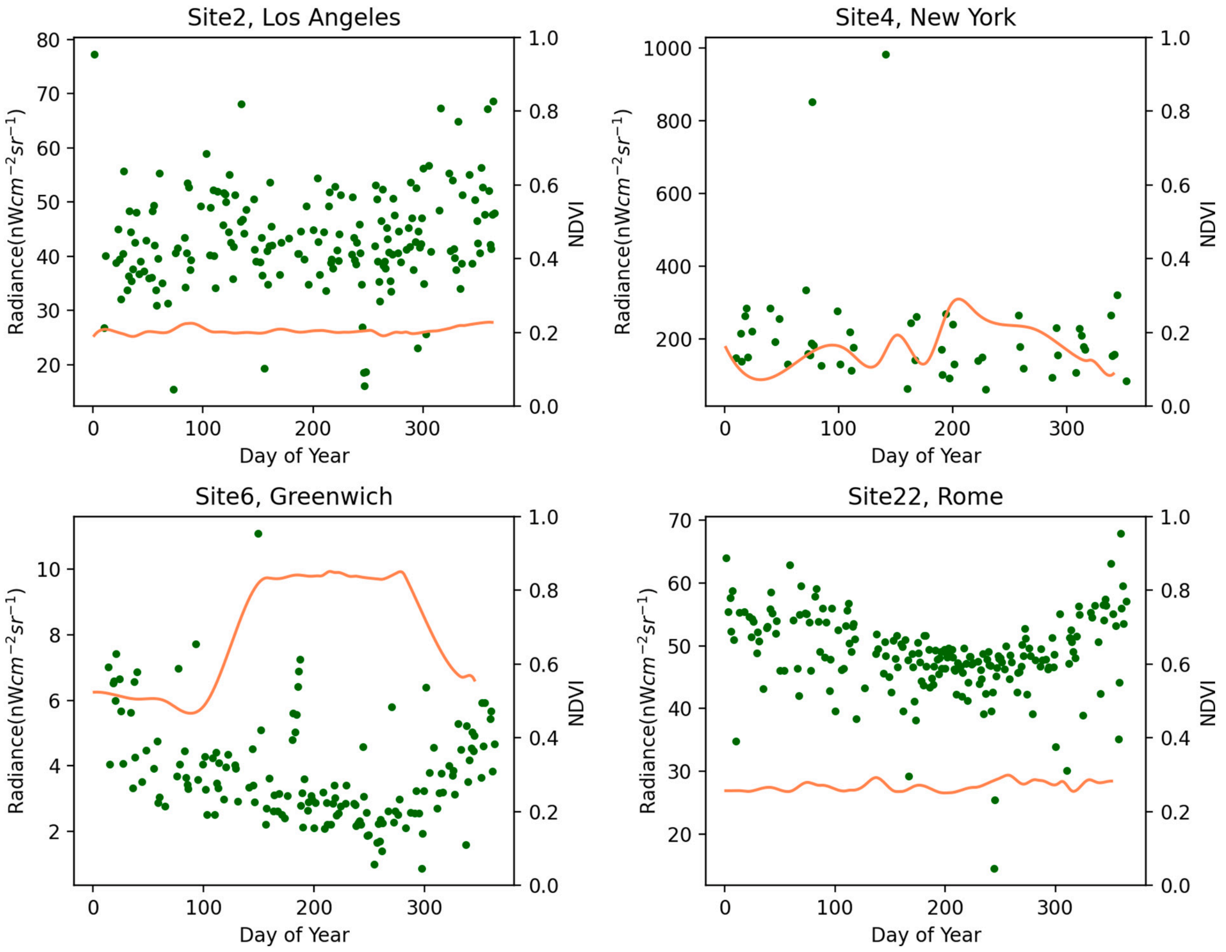

Fig. 16. Temporal snow-free surface NTL radiance (green dots) and vegetation index (NDVI, represented by the orange lines) at Site-2, 4, 6, and 22 in 2018. (For interpretation of the references to colour in this figure legend, the reader is referred to the web version of this article.)

seasonal effect (Xie et al., 2019; Zheng et al., 2019).

Temporal NTL radiance at residential Site-6 was inversely correlated with vegetation index (Fig. 16). NDVI reached 0.8 during the vegetation growing season and dropped to 0.5 during the dormant period. The radiance was around 3 nWcm^{-2} sr^{-1} during the leaf-on period and doubled during the leaf-off period. Site-4 is located at the commercial center of New York City with high-rise buildings. The magnitude and seasonal vegetation variation of NDVI were low compared to Site-6. The temporal NTL radiance of this site was stable indicating nominal impacts by vegetation. The vegetation of Site-2 is evergreen without seasonal variation and NTL radiance was stable within one year.

Evident seasonal NTL radiance was found at Site-22, where vegetation NDVI was steady without seasonal changes. The seasonal NTL radiance variation was not caused by snow since only one snowfall happened in Rome on Feb 26 in 2018 and the snow melted within one week. Human activities could be the driver of seasonal NTL radiance changes at this location. Chen et al. (2019b) also noted that the NTL seasonality was impacted by human activities over different land-use types across Shanghai. Both Site-2 and Site-22 are located at a homogenous residential area with similar NTL radiance (ranging from 30 to 60 nWcm^{-2} sr^{-1}). The NTL radiance of Site-2 is more scattered than Site-22 with larger variation among adjacent days.

3.7. Snow effect

Currently, for Collection V001, the nighttime snow/ice flag in NASA VIIRS Collection1 comes from National Snow & Ice Data Center (NSIDC) and was derived from Brightness Temperature measured by Special Sensor Microwave Imager/Sounder (SSMIS) onboard DMSP (Armstrong and Brodzik, 2001). The coarse 25 km spatial resolution snow product results in large areas of leakage and false alarms (Fig. 17). Misclassification of snow significantly impacts surface NTL radiance retrieval considering high snow albedo. Daytime moderate spatial resolution (1 km) snow/ice flag from the previous daytime will be used in NASA Collection V002 reprocessing (c. late fall, 2021). This strategy will dramatically reduce spatial snow extent uncertainty. Ephemeral snow might melt quickly; therefore, snow observed on daytime could melt before the following nighttime observation. Surface snow/snow-free status in Black Marble product (VNP46A2) is further refined based on the reflected lunar radiance during moonlit nights. The surface is flagged as snow in VNP46A2 if reflected lunar radiance could be better corrected by snow BRDF/albedo than snow-free BRDF/albedo.

As was shown in Fig. 9, reflected lunar radiance is around 23 nWcm^{-2} sr^{-1} during full moon night with an albedo of 0.8 (characteristic of a snow surface). The albedo value of partial snow surface is less than pure snow albedo varying with snow cover fraction. The relative change (Eq. 3) of retrieved lunar BRDF-corrected NTL radiance (i.e., using incorrect surface albedo because of snow flag misclassification) is listed in Table 3. The relative change by misused snow albedo is relatively low ($<$ 6%) during moon-free nights. Conversely, the snow-contaminated surface reflected artificial light is enhanced by reflected lunar radiance during moonlit nights, with the most dramatic differences produced on strong moonlit nights coupled with significantly incorrect surface albedo assumptions, as expected. The retrieved surface NTL radiance is 78.4% higher than the actual radiance for snow surface with 0.8 albedo, particularly if the surface is misclassified as snow-free

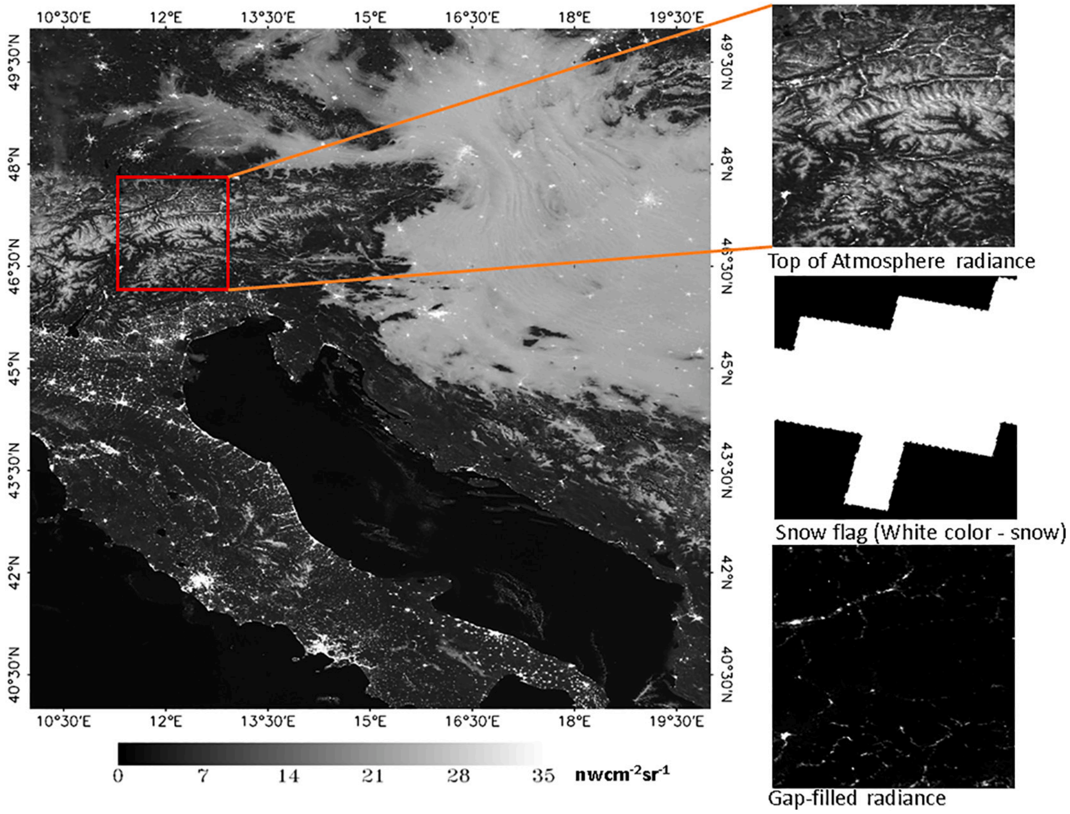

Fig. 17. TOA, gap-filled lunar BRDF-corrected DNB radiance, and snow flag (VNP35 collection 1) on DOY 352 in 2013 in tile h19v04.

and the DNB albedo is set to a snow-free value of 0.1.

3.8. Geometric effect

The geolocation accuracy of NASA VIIRS swath products has a mean residual of 2 m with a root mean square error of less than 70 m along track and 60 m along scan direction (Wolfe et al., 2013). The NASA Black Marble products grid 750 m footprint DNB observations to 15 arc *sec* geographic latitude/longitude pixel. Gridding artifacts resulting from a mismatch between a grid cell and observation footprint increase the geolocation uncertainty (Tan et al., 2006; Campagnolo et al., 2016). The spatial coverage of 15 arc sec geographic Lat/Lon grid ranges from 463 m at the equator to less than 100 m at 80-degree latitude. Therefore the signal of each pixel contains information from the area out of the grid coverage. As such, as a good practice, a 3 × 3-pixel averaging window is recommended for temporal analysis (Román et al., 2018). NTL radiance intensity varies dramatically over different urban regimes with high heterogeneity (Li et al., 2020). Here we evaluated the NTL heterogeneity with several spatial scales averaging windows such as single-pixel, 3 × 3, 5 × 5 and 7 × 7 window regions.

The spatial ranges (a) of the four sites varied from 562 m (Site-13 Beijing) to 726 m (Site-2 Los Angeles) for 2 km subset statistics, and were larger than the established 15 arc sec pixel spatial coverage of the VNP46 product. This indicates that higher temporal NTL radiance variation is expected based on a single pixel. Site-13 was the most homogeneous among the four sites. The sill values of three spatial scales (2 km by 2 km, 3.5 km by 3.5 km, and 5 km by 5 km) at Site-13 were close, and the range was the smallest compared to the other three sites. The range of Site-2 Los Angeles was the largest, and street lines were much brighter than residential houses (Fig. 18). The spatial heterogeneity of Site-22 Rome is close to Site-13 Beijing with slightly higher sill values (4000) compared to Beijing (3000) using a larger spatial statistics subset. Site-21 Rome urban center had the highest sill value indicating high radiance variation. The range of this site was larger than 1000 m at a large statistics subset.

We have also evaluated the relationship of radiance and VZA with different spatial averaging window sizes as shown in Fig. 19. The distribution of different spatial scales radiance of Site-13 is similar, with nearly no change of CV values (Fig. 19). The spatial scaling effect is most significant at Site-21. The CV of Site-21 dropped from 0.28 at a single pixel, to 0.18 at 3 by 3 pixels average, and kept stable from 5 by 5 to 7 by 7 average (CV = 0.15). NTL radiance variation slightly decreased by averaging more pixels at Site-22. The variation of radiance at Site-2 was stable up to 5 by 5 pixels averaging while increased by averaging 7 by 7 pixels, indicating that NTL radiance is homogeneous within 5 by 5 pixels range and becomes heterogeneous over a larger area with more low values below 30 $nWcm^{-2}$ sr^{-1}.

3.9. Aurora

Aurora is one of the major ephemeral extraneous light emissions at high latitude (Newell et al., 2014). Aurora oval spatial coverage is temporarily enlarged by a geomagnetic storm. The size, location, and shape of aurora oval and localized aurora could change in a short time (Frey, 2007). Aurora is most likely to be captured and classified as outliers in Black Marble product. Besides the radiance from the aurora itself, a broad area of the surface could be lighted up by reflecting downwelling aurora irradiance even with no aurora above the sky (Fig. 20). The correction of surface reflected aurora radiance is challenging since downward aurora irradiance is unknown and it varies dramatically. Fig. 20 showed the land surface was lighted up by aurora during the moon-free night to exclude the lunar effect for tile h20v02 on DOY 74, 2018. The maximum radiance from aurora was 66.3 $nWcm^{-2}$ sr^{-1} of this tile from the year 2012 to 2019. Land surface reflected aurora radiance in proximity to aurora area was up to approximate 3.5 $nWcm^{-2}$ sr^{-1} on DOY 74, 2018, and DOY 319, 2012.

Table 3

Relative change of radiance estimated at 50 nWcm^{-2} sr^{-1} TOA DNB, 45 degree Lunar Zenith Angle (LZA), 0 degree VZA, and lunar irradiance of 0 (moon-free), 50 (partial moon), and 140 (full moon) nWcm^{-2}.A climatological AOD value of 0.2 at 550 nm (Yu et al., 2006) was used.

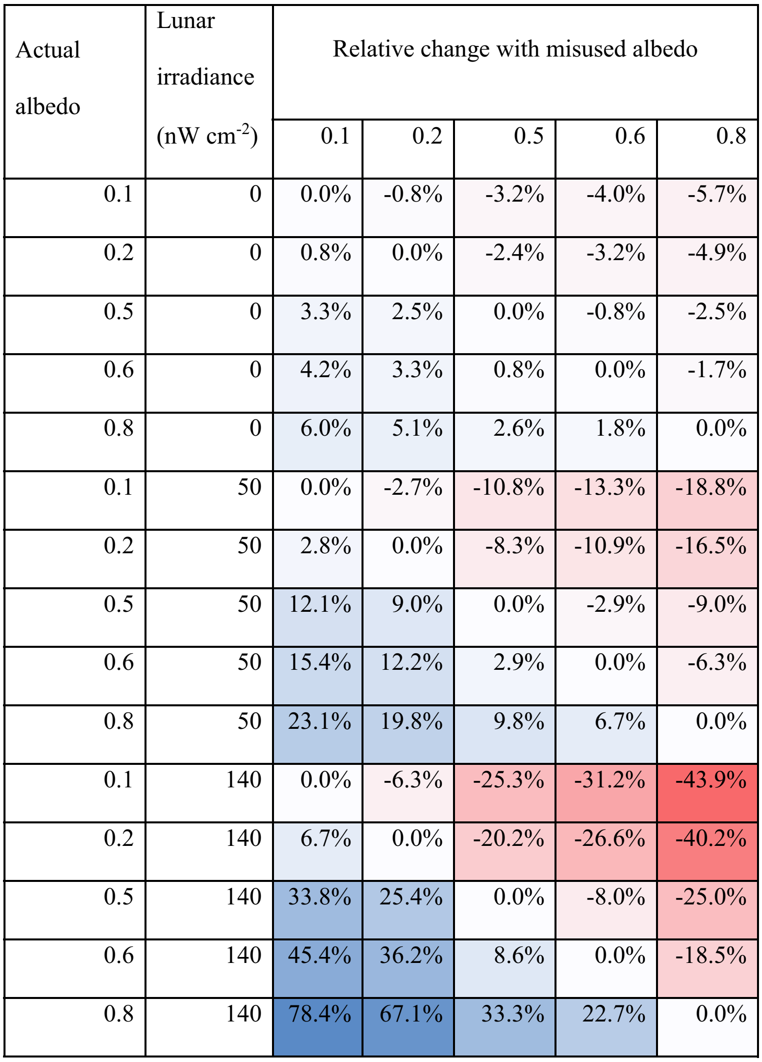

Actual albedo	Lunar irradiance (nW cm^{-2})	Relative change with misused albedo				
		0.1	0.2	0.5	0.6	0.8
0.1	0	0.0%	-0.8%	-3.2%	-4.0%	-5.7%
0.2	0	0.8%	0.0%	-2.4%	-3.2%	-4.9%
0.5	0	3.3%	2.5%	0.0%	-0.8%	-2.5%
0.6	0	4.2%	3.3%	0.8%	0.0%	-1.7%
0.8	0	6.0%	5.1%	2.6%	1.8%	0.0%
0.1	50	0.0%	-2.7%	-10.8%	-13.3%	-18.8%
0.2	50	2.8%	0.0%	-8.3%	-10.9%	-16.5%
0.5	50	12.1%	9.0%	0.0%	-2.9%	-9.0%
0.6	50	15.4%	12.2%	2.9%	0.0%	-6.3%
0.8	50	23.1%	19.8%	9.8%	6.7%	0.0%
0.1	140	0.0%	-6.3%	-25.3%	-31.2%	-43.9%
0.2	140	6.7%	0.0%	-20.2%	-26.6%	-40.2%
0.5	140	33.8%	25.4%	0.0%	-8.0%	-25.0%
0.6	140	45.4%	36.2%	8.6%	0.0%	-18.5%
0.8	140	78.4%	67.1%	33.3%	22.7%	0.0%

3.10. Addressing missing data gaps

The gaps in daily Black Marble nighttime light products are mainly caused by cloud contaminated areas. Potential outliers due to cloud and snow misclassification and model retrieval failures also reduce the frequency of high-quality NTL retrievals. In particular, high latitude regions suffer from solar contamination during the summertime. Improvement of cloud accuracy could reduce cloud contamination and rescue clear-sky observations misclassified as a cloud. An accurate snow flag could also reduce outliers and increase high-quality retrievals. With the launch of NOAA-20 (JPSS-1) in 2017 and the coming JPSS-2/3/4 series satellites, more clear sky observations would be available by combining multi-satellite measurements. To illustrate, in Fig. 21, no NTL data were available over the northern part of tile h10v04 on DOY 141, 2019 due to the low solar zenith angle of S-NPP observations. However, the gaps in the S-NPP Black Marble product were filled with higher-quality observations from NOAA-20 in the same orbit, but 50 min apart in time. We also found that combining multi-satellite VIIRS DNB observations enables the generation of view-angle consistent temporal datasets, thus reducing the uncertainty resulted from the three-dimensional structure of urban corridors. As illustrated in Fig. 22, our global daily science test run in 2019 showed that combining nighttime observations from Suomi-NPP and NOAA-20 would lead to (1) a global net increase in ‘confidently-clear’ land pixels of ~6%, (2) regional daily increases in confidently-clear pixels reaching up to 18%, and (3) minor but persistent improvements (< 5%) at high latitudes during the Summer months when midnight sun conditions develop.

4. Discussion

Using a stratified global sample of well-characterized sites, we disentangled the uncertainties to contain the “one-to-many” relationship inherent to daily NTL time series data. For example, the Los Angeles metropolitan sites (i.e., Site-1, Site-2, and Site-3, in Table 1) exhibited no vegetation/snow effects nor any seasonal pattern, since these sites have weakly varying seasonal vegetation and receive no snowfall. The average NTL radiance from an upscaled 3 × 3 pixel window was also used to evaluate the uncertainty corresponding to angular, aerosol, lunar, and vegetation effects. We found that the geostatistical range of various sampled sites (e.g., Site-2, 13, 21, and 22, in Table 1) was larger

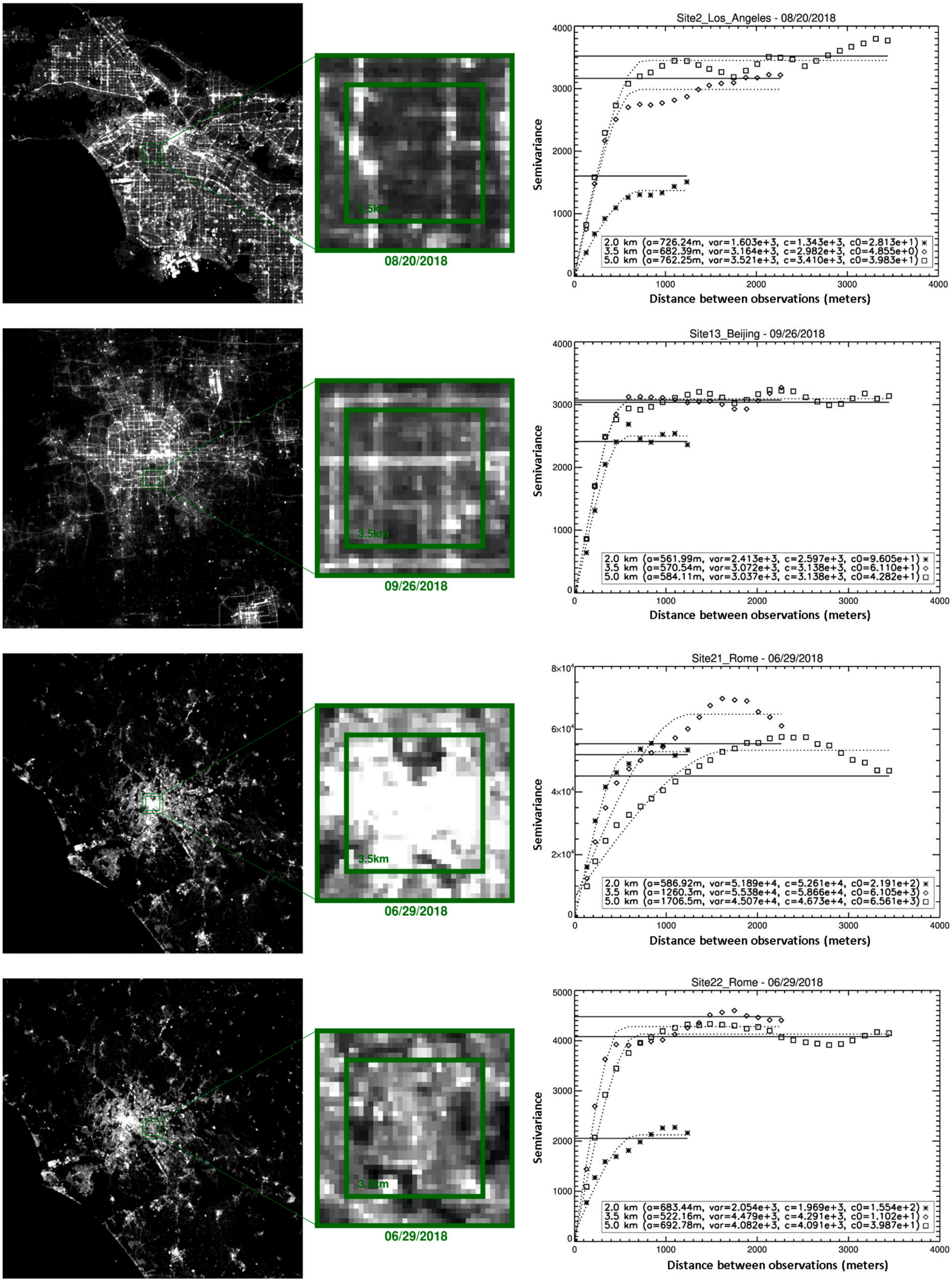

Fig. 18. Luojia-1 NTL and corresponding semivariogram functions, variogram estimator (points), spherical model (dotted curves), and sample variance (solid straight lines) using regions of 2.0 km (asterisks), 3.5 km (diamonds), and 5.0 km (squares), at Site-2 on August 20, 2018, Sit-13 on September 26, 2018, Site-21 on June 29, 2018, and Site-22 on June 20, 2018.

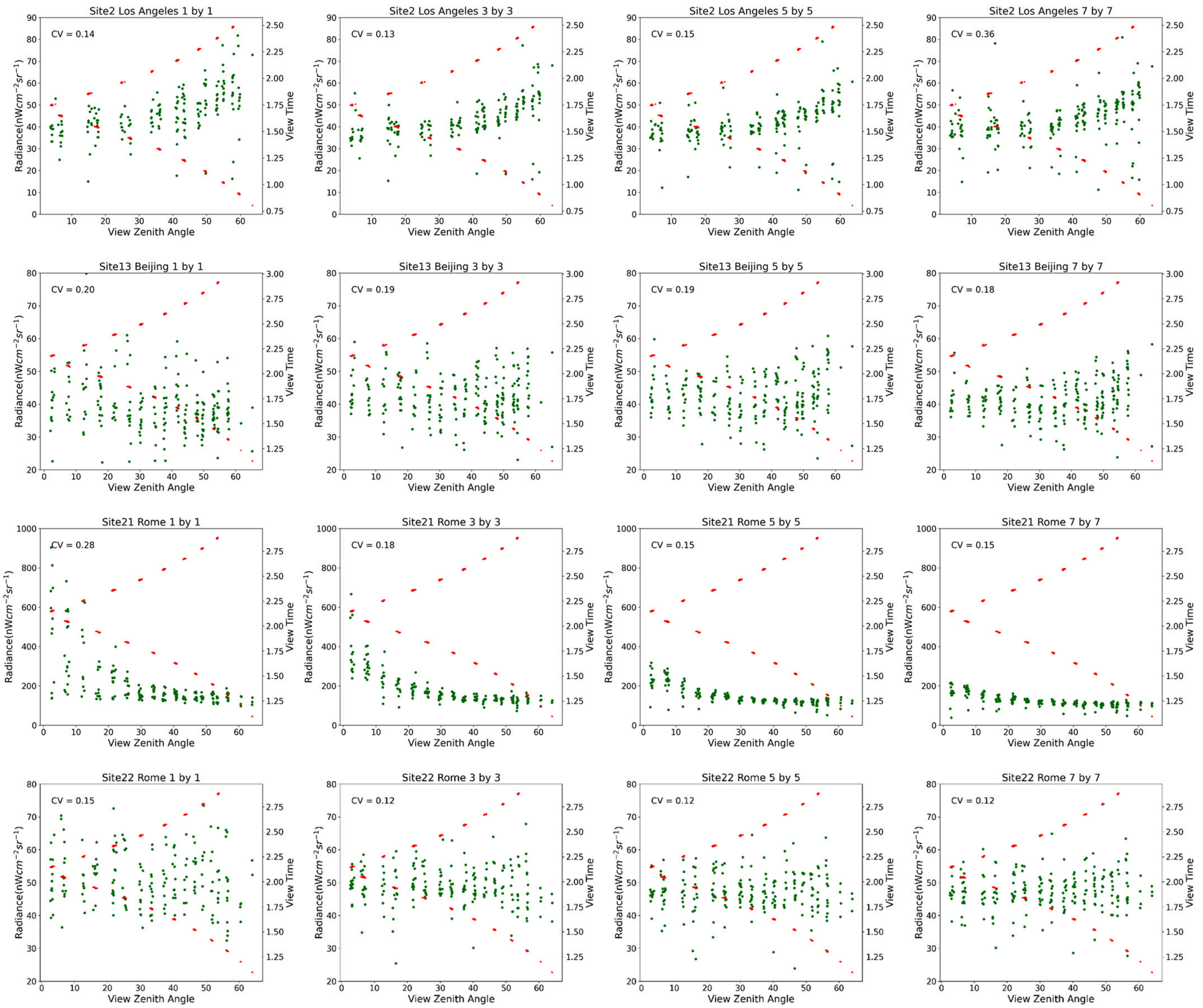

Fig. 19. Relationship of radiance and VZA at different spatial scales at Site-2, 13, 21, and 22 in 2018. Red dots are view time and green dots represent VNP46A2 NTL radiance. (For interpretation of the references to colour in this figure legend, the reader is referred to the web version of this article.)

than 560 m; thus indicating that applying a spatial averaging window effectively reduces the geometric effect. Since the data acquisition time is always nearly the same for nadir looks from this sun-synchronous satellite observations, diurnal changes do not account for the observed nadir's radiance variation.

The three-dimensional structure of vegetation canopies can block or modulate the character of upwelling NTL lights, particularly at more oblique view geometries. As with lunar BRDF-artifacts, quantifying this three-dimensional 'vegetation effect' is inherently complicated, depending on additional factors, e.g., vegetation albedo and urban canopy structure, both of which vary over space and time. The vegetation albedo from both trees and grass affects the reflected artificial lights. For instance, in the case of deciduous vegetation regions, we found that NTL radiance during the leaf-off period can be three times higher than the radiance during the leaf-on season (Fig. 16 Site-6). Researchers should therefore be aware of how NTL time series are affected by these higher-order seasonal effects, particularly over areas with deciduous vegetation, when attributing temporal differences in NTL to various parameters of interest.

We also introduced a new uncertainty metric, the NDHD$_{NTL}$, derived from the hotspot and darkspot NTL radiance to estimate the angular characteristics of NTL with respect to viewing geometry. Using this new metric we were able to confirm that the VZA effect is more significant over dense commercial areas than over residential/rural areas, with NDHD$_{NTL}$ values up to 0.75 over the commercial areas. NTL radiance decreased with increasing VZA over commercial areas while the opposite relationship was found over residential areas. Conversely, the VAA effect played a minor role in influencing the NTL radiance and was only noticeable across areas outside of the cities' suburban area. (Li et al., 2019; Tong et al., 2020). The VAA effect mainly results from atmospheric scattering by NTL emissions around the urban edge, and thus the magnitude of the VAA effect is strongly dependent on the intensity of the urban edge radiance and the aerosol turbidity near this interface. NTL radiance was positively correlated with building heights with R^2 of 0.388 in Los Angeles, but the relationship was weak over tall buildings (Fig. 6 (c)). Conversely, we found that the relationship (R^2) between building heights and NTL radiance was not significant with VZA and VAA. The NTL radiance varied greatly at some sites for a given VZA (Fig. 19). This phenomenon also occurred at sites without vegetation and snow effect (e.g., Fig. 19 Site-2). The variation at a fixed VZA

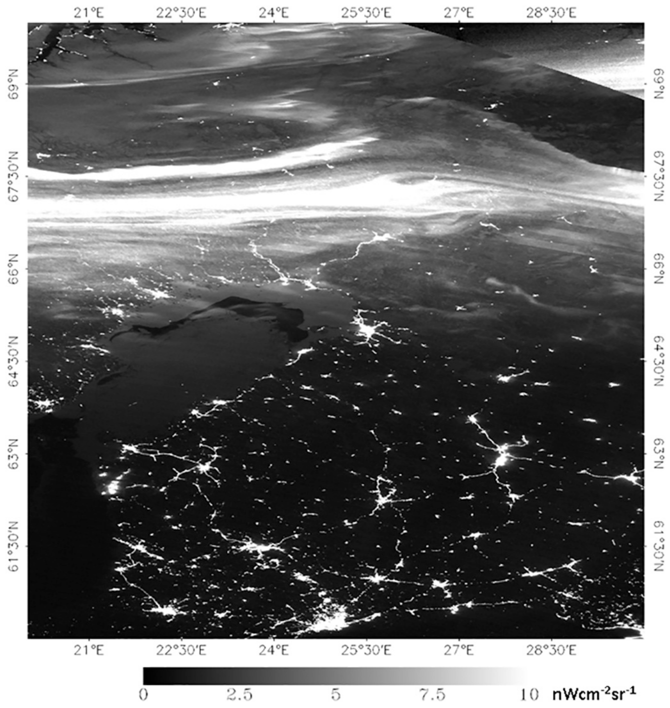

Fig. 20. Aurora (northern part of the tile) in tile h20v02 on DOY 74 in 2018.

decreased at coarser spatial resolution, particularly across commercial urban centers (e.g., Fig. 19, Site-21, Rome), therefore the geometric error partially explains the variation. Undetected clouds could significantly influence the NTL radiance and contribute to the one-to-many relationship. The contribution of airglow natural light to this relationship is minor since the airglow radiance is mostly less than 0.5 nWcm^{-2} sr^{-1}(Coesfeld et al., 2020). NASA's Black Marble uses daytime AOD as input into the atmospheric correction process since a routine nighttime AOD product is currently not available. Assuming a climatological AOD value of 0.2 at 550 nm and a dominant urban surface albedo of 0.15 (Fig. 7), atmospheric NTL correction adjusts the radiance by 5% to 12% for retrievals based on near-nadir and off-nadir view-geometries, respectively (Fig. 13). We found that the difference between daytime and nighttime AOD is less than 0.1 (Figs. 11 and 12). The effect of 0.1 different AOD on radiance is less than 5% (Fig. 13) which is much less than the NTL radiance range of the same VZA (e.g., Figs. 2 and 19). Thus, while atmospheric correction is not a dominant factor in NTL uncertainty, it is still needed when conducting quantitative assessments directly from daily NTL time series, particularly those involving low-lit sources, e.g., rural areas and informal settlements. On the other hand, variations caused by human activities and different satellite overpass time contributed to most of the observed NTL variation, requiring further evaluation.

NASA's Black Marble uses an algorithm processing scheme that removes the contribution of reflected lunar radiance. The algorithm is based on surface BRDF/albedo retrieval since land surface reflectance is anisotropic. We have also quantified the magnitude of snow, cloud, and AOD effects based on radiative transfer model simulation (Fig. 9, Fig. 13, and Table 3). The reflected lunar radiance during full moon periods, for example, is about 5 nWcm^{-2} sr^{-1} for a 0.15 albedo surface, but can exceed 25nWcm^{-2} sr^{-1} for snow-covered surfaces. Retrieved surface NTL radiance over a fully snow-covered surface could be 78.4% higher than the actual value if misclassified as snow-free during full moon conditions, underscoring the importance of correct surface characterization. We also characterized the influence of high aerosol loadings on NTL. For example, NTL radiance of 50 nWcm^{-2} sr^{-1} surfaces could attenuated over 30% by an atmosphere having a visible AOD of 0.8.

Likewise, NTL retrievals are particularly sensitive to obscuration from clouds, especially across commercial and residential areas, both during moon-free and moonlit nights. Cloud misclassification is one of the major sources of NTL outliers. Cloud-contaminated pixels could completely block artificial light radiance during the moon-free night, while also raising NTL radiance to above 25 nWcm^{-2} sr^{-1} over natural regions.

Though the effects of stray light contamination in DNB data have been well documented and largely corrected (Chen et al., 2019a; Lee and Cao, 2016), users should continue to use caution when assessing changes in NTL data with solar zenith angle close to the horizon ($\text{SZA} < 108^\circ$). Likewise, transition in recent years of city light sources types (e.g., light-emitting diode (LED) lights) is another element that should be studied (Bará et al., 2019; Falchi et al., 2016; Kyba et al., 2017; Sánchez de Miguel et al., 2019). Whereas the VIIRS DNB does not capture the light in the range of 400 to 500 nm, its broad spectral bandpass vis-à-vis the broad emissions spectra of LED lights does enable it to capture these changes. Indirect methods may also be possible, such as observable reductions of DNB radiance as High Pressure Sodium (HPS) transition to LED lights (Kyba et al., 2017). Therefore users should be cautious when pursuing applications based on DNB observations that depend strongly

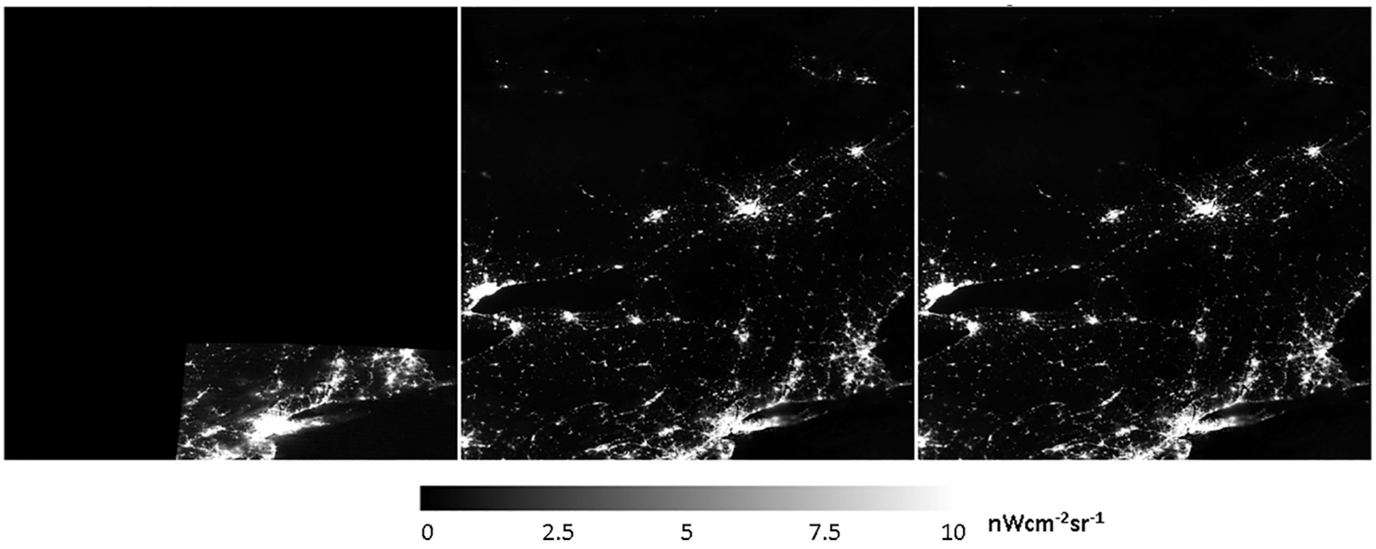

Fig. 21. S-NPP (left), NOAA-20 (middle), and S-NPP + NOAA-20 (right) TOA DNB radiance of tile h10v04 on DOY 147 in 2019.

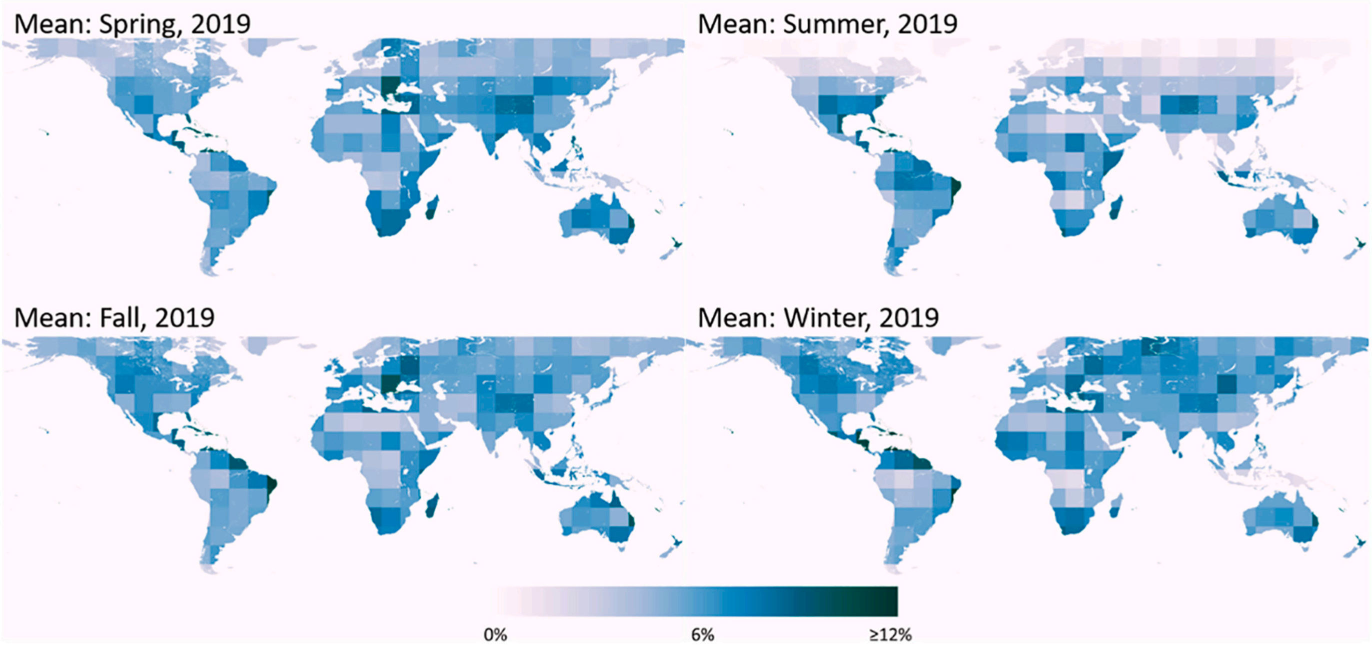

Fig. 22. Global daily science test run for 2019 (290 Black Marble Level 3 tiles × 365 days = 105,850 samples) quantifies the mean seasonal increase (%) in 'confidently-clear' pixels from combined S-NPP/NOAA-20 retrievals (upcoming VCD46 product suite).

on NTL coloration, such as the recently documented impacts of COVID-19 on urban activities (Bustamante-Calabria et al., 2021; Elvidge et al., 2020; Ghosh et al., 2020; Jechow and Hölker, 2020; Liu et al., 2020a; Straka et al., 2021). Other sources of NTL observations like the International Space Station (ISS) or the Jilin-1 satellite can significantly improve the evaluation of the VIIRS DNB for COVID-19 impact assessments both in terms of spatial and spectral information. Likewise, having a geostationary nighttime measurement platform, e.g. the next generation of US measurements from Geostationary and Extended Orbits, (GEO-XO) would significantly advance the science of Earth at Night, while reducing the uncertainties such as cloud errors, angular effect, and diurnal NTL variation.

We found that NTL radiance of locations close to water bodies could also be enhanced by water reflected NTL, particularly at the glint geometry when considering moonlight or waterways below illuminated bridges, etc. Researchers should also keep in mind that the Suomi-NPP and NOAA-20 local overpass time (despite being ~01:30 near the equator) is in fact variable, particularly at high latitude regions where multi-observations could be acquired per night. The artificial light variation through one night could be equally large (Kyba et al., 2020, 2015; Li et al., 2020; Sánchez de Miguel, 2015).

Previous studies found that Monthly NTL radiance derived from TOA DNB has a standard deviation of 20% relative to the median value (Coesfeld et al., 2018). We show that monthly or annual composite NTL could also be further biased when uncertainties are not well quantified, and outliers were not filtered out. Lunar BRDF and atmospheric corrected NTL reduce the uncertainty on monthly and annual composite caused by the moon and atmospheric parameters. The use of temporal composites, separating snow-covered and snow-free conditions, could also avoid snow-related effects on the final products. Likewise, the angular effect can be effectively addressed by selecting view angle consistent observations.

Outliers can be reduced by using a more conservative nighttime cloud mask, though more available observations are required to capture abrupt short-term changes. Quantifying short-time changes is challenging considering the uncertainties, especially during extended periods of cloud coverage. For example, leakage of cloud detection, which blocks the artificial light, could result in false detection of a power outage (Román et al., 2019). False power outage recovery could also be observed if cloud and lunar illumination were not corrected during moonlit nights. We demonstrate that combining multi-sensor VIIRS DNB observations such as Suomi-NPP and NOAA-20, could further reduce persistent gaps and reduce uncertainties inherent in using NTL observations across fixed view geometry ranges.

5. Conclusions

This study presented a methodology to identify and quantify the key factors contributing to retrieval uncertainties in NASA's Black Marble daily nighttime lights (NTL) product suite. Specifically, we quantified the NTL radiance uncertainty arising from view geometry, surface BRDF/albedo, moonlight, aerosol, cloud, snow, vegetation, geometric, and aurora. We then summarized how these known factors contribute, both jointly and independently, to variations in NTL time series data, that are unrelated to human activities.

Twenty-four globally-distributed sites in seven metropolitan areas representing a gradient of commercial urban center – residential – rural areas with different vegetation conditions and building heights were selected to evaluate the NTL uncertainty. Generally commercial urban centers showed high NTL variation particularly at near-nadir VZA and the highest angular effect. The NTL radiance decreased toward higher VZA at commercial urban center while residential and rural areas usually showed the increased trend. Rural sites had the highest CV though the SD values are low due to low NTL radiance. The lunar effect is the highest at rural sites and decreases toward higher NTL radiance regions. The vegetation effect is the most over suburban residential sites with deciduous trees. The geometric effect can be effectively reduced by applying a spatial averaging window.Angular and atmospheric effects dominate NTL radiance uncertainty, while snow/cloud misclassification and severe aerosol pollution are the main drivers of outliers. Angular effect impacts the most over the urban center where NTL radiance at nadir look could be tripled higher than off-nadir observations. Aerosol loadings with AOD larger than 0.8 reduce the NTL radiance by more than 30% over low albedo surface (Fig. 13). The retrieved NTL radiance over predominantly snow-covered surfaces could be 78.4% higher than the actual value because of snow misclassification. Retrieved NTL radiance at snow-free surfaces, in turn, could be 43.9% lower than actual value by using snow albedo.

Seasonal NTL radiance variation could be related to snow cover, albedo, and vegetation (Levin, 2017; Levin and Zhang, 2017). During winter months, high snow albedo enhances NTL radiance by increasing the reflected lunar radiance and reflected artificial light. Low gap fraction vegetation canopy during growing season blocks more light than the leaf-off period. The vegetation effect is more prominent in suburban/rural areas than in urban centers (Fig. 16). The lunar irradiance impact follows the monthly moon phase cycle and is more significant during full moon periods. However, we found that the influence is subtle over high artificial light radiance areas. The S-NPP and NOAA-20 orbit repeat every 16 days. Therefore VIIRS DNB observations with the same view angle for each location could be acquired every 16 days, reducing the angular effect by choosing observations with the same view angles for temporal analysis.

DNB pixels contaminated by the aurora borealis radiance can reach values higher than 60 nWcm-2 sr-1. Further statistics covering a larger area and temporal range are needed to evaluate the aurora effect and constrain its influence from the NTL time series. In particular, careful attention should be placed around transition zones near the aurora boundary, where the effect results in retro-reflectance (i.e., surface illumination by reflecting downward aurora irradiance (Miller et al., 2013)).

The impact of the abovementioned factors on uncertainty is coupled. Reflected lunar radiance is enhanced over snow-covered surfaces with high albedo. Also, the increased reflected light further raises the atmospheric scattered light. Cloud contamination is also dissimilar during moon-free and moonlit nights – artificial lights are reduced by cloud blocking during the moon-free night, but could also increase over rural/suburban regions during moonlit periods. Misclassification of cloud and snow flags introduces large uncertainty to NTL radiance. Accordingly, the current NASA Collection V001 lunar BRDF-corrected NTL radiance (VNP46A2) is considered ‘Beta’ until ongoing issues with nighttime AOD, snow, and cloud flags can be addressed in the near future.

In summary, to reduce the sources of measurement error and retrieval uncertainty and address persistent data gaps, we recommend (1) using lunar-BRDF adjusted and atmospherically corrected NTL (i.e., as identified as high-quality retrievals in the VNP46 QA fields), (2) improving snow cover and cloud masks accuracy, (3) characterizing seasonal variations due to vegetation and snow, (4) reducing geometric effects (e.g., using a spatial window), (5) combining angularly-consistent NTL observations from multiple VIIRS instruments especially before making assessments of temporal NTL change, and (6) being mindful of surface-reflected radiance from aurora events at mid-to-high latitudes. These findings underpin the level of technical effort necessary to establish a stable NTL time series record of sufficient data quality for quantitative analyses. Users should be fully aware of these uncertainty factors, particularly when employing Black Marble NTL products in peer-reviewed research and embarking upon various application studies. A necessary step includes using QA flags (provisioned through VNP46A1 and key upstream data products) and additional data layers describing the state of nighttime snow, cloud, and aerosol conditions. Users also need to be aware that calibration stability and consistency are essential to ensure a science-quality NTL time series.

We conclude by noting that further refinements to NASA’s Black Marble Product Suite, reflecting the various refinements presented in this study, are being implemented as part of the next VIIRS Land Science Collection V002 reprocessing cycle. We advise users of these data to pay close attention to the recent updates from NASA’s Land Science Investigator-led Processing System regarding archival, distribution, science data product releases (add data DOI ref.: https://ladsweb.modaps.eosdis.nasa.gov/missions-and-measurements/products/VNP46A2/).

Declaration of Competing Interest

The authors declare that they have no known competing financial interests or personal relationships that could have appeared to influence the work reported in this paper.

Acknowledgments

The authors received funding from NASA’s Applied Sciences program, NASA’s Earth Science Data and Information Systems (ESDIS) project, NASA’s Suomi-NPP Project, NASA’s Terra/Aqua/Suomi-NPP program and NASA’s Remote Sensing Theory for Earth Science program, which supported our project under the following RTOP and NSSC grants: NNH16ZDA001N-GEO16-0055, NNH17ZDA001N-TASNPP17-0007. 80NSSC19K1080, 80NSSC20K1083, and 80NSSC20K1748. The funders had no role in study design, data collection and analysis, decisions to publish, or preparation of the manuscript. We thank the (PI(s) and Co-I(s)) and their staff for establishing and maintaining the 37 AERONET sites used in this investigation. We also thank University of Dhaka, DEWA Research center, and Prof. Toshihiko Takemura from Kyushu University to co-maintain the Dhaka_University, DEWA_ResearchCentre, and Fukuoka AERONET sites respectively.

References

Ackerman, S.A., Strabala, K.I., Menzel, W.P., Frey, R.A., Moeller, C.C., Gumley, L.E., 1998. Discriminating clear sky from clouds with MODIS. J. Geophys. Res. Atmos. https://doi.org/10.1029/1998JD200032.

Amaral, S., Câmara, G., Monteiro, A.M.V., Quintanilha, J.A., Elvidge, C.D., 2005. Estimating population and energy consumption in Brazilian Amazonia using DMSP nighttime satellite data. Comput. Environ. Urban. Syst. https://doi.org/10.1016/j.compenvurbsys.2003.09.004.

Armstrong, R.L., Brodzik, M.J., 2001. Recent northern hemisphere snow extent: a comparison of data derived from visible and microwave satellite sensors. Geophys. Res. Lett. https://doi.org/10.1029/2000GL012556.

Bará, S., Rigueiro, I., Lima, R.C., 2019. Monitoring transition: expected night sky brightness trends in different photometric bands. J. Quant. Spectrosc. Radiat. Transf. https://doi.org/10.1016/j.jqsrt.2019.106644.

Barreto, A., Román, R., Cuevas, E., Pérez-Ramírez, D., Berjón, A.J., Kouremeti, N., Kazadzis, S., Gröbner, J., Mazzola, M., Toledano, C., Benavent-Oltra, J.A., Doppler, L., Juryšek, J., Almansa, A.F., Victori, S., Maupin, F., Guirado-Fuentes, C., González, R., Vitale, V., Goloub, P., Blarel, L., Alados-Arboledas, L., Woolliams, E., Taylor, S., Antuña, J.C., Yela, M., 2019. Evaluation of night-time aerosols measurements and lunar irradiance models in the frame of the first multi-instrument nocturnal intercomparison campaign. Atmos. Environ. https://doi.org/10.1016/j.atmosenv.2019.01.006.

Bennie, J., Davies, T.W., Duffy, J.P., Inger, R., Gaston, K.J., 2015. Contrasting trends in light pollution across Europe based on satellite observed night time lights. Sci. Rep. https://doi.org/10.1038/srep03789.

Berkoff, T.A., Sorokin, M., Stone, T., Eck, T.F., Hoff, R., Welton, E., Holben, B., 2011. Nocturnal aerosol optical depth measurements with a small-aperture automated photometer using the moon as a light source. J. Atmos. Ocean. Technol. https://doi.org/10.1175/JTECH-D-10-05036.1.

Bustamante-Calabria, M., de Miguel, A.S., Martín-Ruiz, S., Ortiz, J.L., Vílchez, J.M., Pelegrina, A., García, A., Zamorano, J., Bennie, J., Gaston, K.J., 2021. Effects of the covid-19 lockdown on urban light emissions: ground and satellite comparison. Remote Sens. https://doi.org/10.3390/rs13020258.

Campagnolo, M.L., Sun, Q., Liu, Y., Schaaf, C., Wang, Z., Román, M.O., 2016. Estimating the effective spatial resolution of the operational BRDF, albedo, and nadir reflectance products from MODIS and VIIRS. Remote Sens. Environ. https://doi.org/10.1016/j.rse.2015.12.033.

Cao, C., Bai, Y., 2014. Quantitative analysis of VIIRS DNB nightlight point source for light power estimation and stability monitoring. Remote Sens. https://doi.org/10.3390/rs61211915.

Cao, C., Bai, Y., Wang, W., Choi, T., 2019. Radiometric inter-consistency of VIIRS DNB on Suomi NPP and NOAA-20 from observations of reflected lunar lights over deep convective clouds. Remote Sens. https://doi.org/10.3390/rs11080934.

Cao, C., Zhang, B., Shao, X., Wang, W., Uprety, S., Choi, T., Blonski, S., Gu, Y., Bai, Y., Lin, L., Kalluri, S., 2021. Mission-long recalibrated science quality suomi npp viirs radiometric dataset using advanced algorithms for time series studies. Remote Sens. https://doi.org/10.3390/rs13061075.

Chen, X., Nordhaus, W., 2015. A test of the new VIIRS lights data set: population and economic output in Africa. Remote Sens. https://doi.org/10.3390/rs70404937.

Chen, J.M., Menges, C.H., Leblanc, S.G., 2005. Global mapping of foliage clumping index using multi-angular satellite data. Remote Sens. Environ. 97, 447–457. https://doi.org/10.1016/j.rse.2005.05.003.

Chen, Z., Yu, B., Hu, Y., Huang, C., Shi, K., Wu, J., 2015. Estimating house vacancy rate in metropolitan areas using NPP-VIIRS nighttime light composite data. IEEE J. Sel.

Top. Appl. Earth Obs. Remote Sens. https://doi.org/10.1109/JSTARS.2015.2418201.

Chen, H., Xiong, X., Geng, X., Twedt, K., 2019a. Stray-light correction and prediction for Suomi National Polar-orbiting Partnership visible infrared imaging radiometer suite day-night band. J. Appl. Remote. Sens. 13, 1. https://doi.org/10.1117/1.jrs.13.024521.

Chen, Z., Yu, B., Ta, N., Shi, K., Yang, C., Wang, C., Zhao, X., Deng, S., Wu, J., 2019b. Delineating seasonal relationships between Suomi NPP-VIIRS nighttime light and human activity across Shanghai, China. IEEE J. Sel. Top. Appl. Earth Obs. Remote Sens. https://doi.org/10.1109/JSTARS.2019.2916323.

Cho, Y.M., Ryu, S.H., Lee, B.R., Kim, K.H., Lee, E., Choi, J., 2015. Effects of artificial light at night on human health: a literature review of observational and experimental studies applied to exposure assessment. Chronobiol. Int. https://doi.org/10.3109/07420528.2015.1073158.

Coesfeld, J., Anderson, S.J., Baugh, K., Elvidge, C.D., Schernthanner, H., Kyba, C.C.M., 2018. Variation of individual location radiance in VIIRS DNB monthly composite images. Remote Sens. https://doi.org/10.3390/rs10121964.

Coesfeld, J., Kuester, T., Kuechly, H.U., Kyba, C.C.M., 2020. Reducing variability and removing natural light from nighttime satellite imagery: a case study using the VIIRS DNB. Sensors (Switzerland). https://doi.org/10.3390/s20113287.

Coscieme, L., Pulselli, F.M., Bastianoni, S., Elvidge, C.D., Anderson, S., Sutton, P.C., 2014. A thermodynamic geography: night-time satellite imagery as a proxy measure of emergy. Ambio. https://doi.org/10.1007/s13280-013-0468-5.

Elvidge, C.D., Baugh, K.E., Kihn, E.A., Kroehl, H.W., Davis, E.R., Davis, C.W., 1997. Relation between satellite observed visible-near infrared emissions, population, economic activity and electric power consumption. Int. J. Remote Sens. 18, 1373–1379. https://doi.org/10.1080/014311697218485.

Elvidge, C.D., Baugh, K.E., Dietz, J.B., Bland, T., Sutton, P.C., Kroehl, H.W., 1999. Radiance calibration of DMSP-OLS low-light imaging data of human settlements. Remote Sens. Environ. https://doi.org/10.1016/S0034-4257(98)00098-4.

Elvidge, C.D., Ziskin, D., Baugh, K.E., Tuttle, B.T., Ghosh, T., Pack, D.W., Erwin, E.H., Zhizhin, M., 2009. A fifteen year record of global natural gas flaring derived from satellite data. Energies. https://doi.org/10.3390/en20300595.

Elvidge, C.D., Zhizhin, M., Baugh, K., Hsu, F.C., 2015. Automatic boat identification system for VIIRS low light imaging data. Remote Sens. https://doi.org/10.3390/rs70303020.

Elvidge, C.D., Baugh, K., Zhizhin, M., Hsu, F.C., Ghosh, T., 2017. VIIRS nighttime lights. Int. J. Remote Sens. https://doi.org/10.1080/01431161.2017.1342050.

Elvidge, C.D., Ghosh, T., Hsu, F., Zhizhin, M., 2020. The dimming of lights in China during the COVID-19 pandemic. Remote Sens. 12 https://doi.org/10.3390/rs12172851.

Falchi, F., Cinzano, P., Duriscoe, D., Kyba, C.C.M., Elvidge, C.D., Baugh, K., Portnov, B.A., Rybnikova, N.A., Furgoni, R., 2016. The new world atlas of artificial night sky brightness. Sci. Adv. https://doi.org/10.1126/sciadv.1600377.

Frey, H.U., 2007. Localized aurora beyond the auroral oval. Rev. Geophys. https://doi.org/10.1029/2005RG000174.

Gao, B.C., Kaufman, Y.J., 1995. Selection of the 1.375-μm MODIS channel for remote sensing of cirrus clouds and stratospheric aerosols from space. J. Atmos. Sci. https://doi.org/10.1175/1520-0469(1995)052.

Garstang, R.H., 2007. Brightness of clouds at night over a city. Observatory 127, 1–13.

Gaston, K.J., Bennie, J., Davies, T.W., Hopkins, J., 2013. The ecological impacts of nighttime light pollution: a mechanistic appraisal. Biol. Rev. https://doi.org/10.1111/brv.12036.

Ghosh, T., Elvidge, C.D., Hsu, F.C., Zhizhin, M., Bazilian, M., 2020. The dimming of lights in India during the covid-19 pandemic. Remote Sens. https://doi.org/10.3390/rs12203289.

Giles, D.M., Sinyuk, A., Sorokin, M.G., Schafer, J.S., Smirnov, A., Slutsker, I., Eck, T.F., Holben, B.N., Lewis, J.R., Campbell, J.R., Welton, E.J., Korkin, S.V., Lyapustin, A.I., 2019a. Advancements in the aerosol robotic Network (AERONET) version 3 database - automated near-real-time quality control algorithm with improved cloud screening for Sun photometer aerosol optical depth (AOD) measurements. Atmos. Meas. Tech. https://doi.org/10.5194/amt-12-169-2019.

Giles, D.M., Slutsker, I., Schafer, J., Sorokin, M., Smirnov, A., Eck, T.F., Holben, B., Welton, E.J., 2019b. Uncertainty and Bias in AERONET Nighttime AOD Measurements, Abstract A23R-3050 presented at 2019 Fall Meeting, AGU, San Francisco, CA, 9–13 Dec.

Guk, E., Levin, N., 2020. Analyzing spatial variability in nighttime lights using a high spatial resolution color Jilin-1 image – Jerusalem as a case study. ISPRS J. Photogramm. Remote Sens. https://doi.org/10.1016/j.isprsjprs.2020.02.016.

Guo, W., Lu, D., Wu, Y., Zhang, J., 2015. Mapping impervious surface distribution with integration of SNNP VIIRS-DNB and MODIS NDVI data. Remote Sens. https://doi.org/10.3390/rs70912459.

Hofmann, W., Lemke, D., Thum, C., 1977. Balloon-borne infrared telescope for absolute surface photometry of the night sky. Appl. Opt. https://doi.org/10.1364/ao.16.003125.

Hu, S., Ma, S., Yan, W., Hindley, N.P., Xu, K., Jiang, J., 2019. Measuring gravity wave parameters from a nighttime satellite low-light image based on two-dimensional stockwell transform. J. Atmos. Ocean. Technol. https://doi.org/10.1175/JTECH-D-18-0092.1.

Hutchison, K.D., Roskovensky, J.K., Jackson, J.M., Heidinger, A.K., Kopp, T.J., Pavolonis, M.J., Frey, R., 2005. Automated cloud detection and classification of data collected by the visible infrared imager radiometer suite (VIIRS). Int. J. Remote Sens. https://doi.org/10.1080/01431160500196786.

Hutchison, K.D., Iisager, B.D., Hauss, B., 2012. The use of global synthetic data for pre-launch tuning of the VIIRS cloud mask algorithm. Int. J. Remote Sens. https://doi.org/10.1080/01431161.2011.571299.

Jean, N., Burke, M., Xie, M., Davis, W.M., Lobell, D.B., Ermon, S., 2016. Combining satellite imagery and machine learning to predict poverty. Science (80-.). https://doi.org/10.1126/science.aaf7894.

Jechow, A., Hölker, F., 2020. Evidence that reduced air and road traffic decreased artificial night-time skyglow during COVID-19 lockdown in Berlin, Germany. Remote Sens. https://doi.org/10.3390/rs12203412.

Jechow, A., Hölker, F., Kyba, C.C.M., 2019. Using all-sky differential photometry to investigate how nocturnal clouds darken the night sky in rural areas. Sci. Rep. https://doi.org/10.1038/s41598-018-37817-8.

Jiang, W., He, G., Long, T., Liu, H., 2017a. Ongoing conflict makes Yemen dark: from the perspective of nighttime light. Remote Sens. https://doi.org/10.3390/rs9080798.

Jiang, W., He, G., Long, T., Wang, C., Ni, Y., Ma, R., 2017b. Assessing light pollution in China based on nighttime light imagery. Remote Sens. https://doi.org/10.3390/rs9020135.

Jiang, W., He, G., Long, T., Guo, H., Yin, R., Leng, W., Liu, H., Wang, G., 2018. Potentiality of using luojia 1-01 nighttime light imagery to investigate artificial light pollution. Sensors (Switzerland). https://doi.org/10.3390/s18092900.

Joachim, L., Storch, T., 2020. Cloud detection for night-time panchromatic visible and near-infrared satellite imagery. ISPRS Ann. Photogramm. Remote Sens. Spat. Inf. Sci. V-2–2020, 853–860. https://doi.org/10.5194/isprs-annals-v-2-2020-853-2020.

Johnson, R.S., Zhang, J., Hyer, E.J., Miller, S.D., Reid, J.S., 2013. Preliminary investigations toward nighttime aerosol optical depth retrievals from the VIIRS Day/Night Band. Atmos. Meas. Tech. https://doi.org/10.5194/amt-6-1245-2013.

Kopp, T.J., Thomas, W., Heidinger, A.K., Botambekov, D., Frey, R.A., Hutchison, K.D., Iisager, B.D., Brueske, K., Reed, B., 2014. The viirs cloud mask: Progress in the first year of s-npp toward a common cloud detection scheme. J. Geophys. Res. https://doi.org/10.1002/2013JD020458.

Kyba, C.C.M., Garz, S., Kuechly, H., de Miguel, A.S., Zamorano, J., Fischer, J., Hölker, F., 2015. High-resolution imagery of earth at night: new sources, opportunities and challenges. Remote Sens. https://doi.org/10.3390/rs70100001.

Kyba, C.C.M., Kuester, T., De Miguel, A.S., Baugh, K., Jechow, A., Hölker, F., Bennie, J., Elvidge, C.D., Gaston, K.J., Guanter, L., 2017. Artificially lit surface of earth at night increasing in radiance and extent. Sci. Adv. https://doi.org/10.1126/sciadv.1701528.

Kyba, C.C.M., Ruby, A., Kuechly, H.U., Kinzey, B., Miller, N., Sanders, J., Barentine, J., Kleinodt, R., Espey, B., 2020. Direct measurement of the contribution of street lighting to satellite observations of nighttime light emissions from urban areas. Light. Res. Technol. https://doi.org/10.1177/1477153520958463.

Lee, S., Cao, C., 2016. Soumi NPP VIIRS day/night band stray light characterization and correction using calibration view data. Remote Sens. https://doi.org/10.3390/rs8020138.

Lee, S., McIntire, J., Oudrari, H., Schwarting, T., Xiong, X., 2015. A new method for Suomi-NPP VIIRS day-night band on-orbit radiometric calibration. IEEE Trans. Geosci. Remote Sens. https://doi.org/10.1109/TGRS.2014.2321835.

Levin, N., 2017. The impact of seasonal changes on observed nighttime brightness from 2014 to 2015 monthly VIIRS DNB composites. Remote Sens. Environ. https://doi.org/10.1016/j.rse.2017.03.003.

Levin, N., Zhang, Q., 2017. A global analysis of factors controlling VIIRS nighttime light levels from densely populated areas. Remote Sens. Environ. https://doi.org/10.1016/j.rse.2017.01.006.

Levin, N., Ali, S., Crandall, D., Kark, S., 2019. World heritage in danger: big data and remote sensing can help protect sites in conflict zones. Glob. Environ. Chang. https://doi.org/10.1016/j.gloenvcha.2019.02.001.

Levin, N., Kyba, C.C.M., Zhang, Q., Sánchez de Miguel, A., Román, M.O., Li, X., Portnov, B.A., Molthan, A.L., Jechow, A., Miller, S.D., Wang, Z., Shrestha, R.M., Elvidge, C.D., 2020. Remote sensing of night lights: a review and an outlook for the future. Remote Sens. Environ. 237 https://doi.org/10.1016/j.rse.2019.111443.

Li, X., Li, D., 2014. Can night-time light images play a role in evaluating the Syrian Crisis? Int. J. Remote Sens. https://doi.org/10.1080/01431161.2014.971469.

Li, X., Chen, F., Chen, X., 2013a. Satellite-observed nighttime light variation as evidence for global armed conflicts. IEEE J. Sel. Top. Appl. Earth Obs. Remote Sens. https://doi.org/10.1109/JSTARS.2013.2241021.

Li, X., Xu, H., Chen, X., Li, C., 2013b. Potential of NPP-VIIRS nighttime light imagery for modeling the regional economy of China. Remote Sens. https://doi.org/10.3390/rs5063057.

Li, X., Li, D., Xu, H., Wu, C., 2017a. Intercalibration between DMSP/OLS and VIIRS night-time light images to evaluate city light dynamics of Syria's major human settlement during Syrian Civil War. Int. J. Remote Sens. https://doi.org/10.1080/01431161.2017.1331476.

Li, X., Zhang, C., Li, W., Liu, K., 2017b. Evaluating the use of DMSP/OLS nighttime light imagery in predicting PM2.5 concentrations in the Northeastern United States. Remote Sens. https://doi.org/10.3390/rs9060620.

Li, X., Liu, S., Jendryke, M., Li, D., Wu, C., 2018a. Night-time light dynamics during the Iraqi CivilWar. Remote Sens. 10, 1–19. https://doi.org/10.3390/rs10060858.

Li, X., Zhan, C., Tao, J., Li, L., 2018b. Long-term monitoring of the impacts of disaster on human activity using DMSP/OLS nighttime light data: a case study of the 2008 Wenchuan, China Earthquake. Remote Sens. https://doi.org/10.3390/rs10040588.

Li, X., Zhao, L., Li, D., Xu, H., 2018c. Mapping urban extent using Luojia 1-01 nighttime light imagery. Sensors (Basel). https://doi.org/10.3390/s18113665.

Li, X., Ma, R., Zhang, Q., Li, D., Liu, S., He, T., Zhao, L., 2019. Anisotropic characteristic of artificial light at night – systematic investigation with VIIRS DNB multi-temporal observations. Remote Sens. Environ. https://doi.org/10.1016/j.rse.2019.111357.

Li, X., Levin, N., Xie, J., Li, D., 2020. Monitoring hourly nighttime light by an unmanned aerial vehicle and its implications to satellite remote sensing. Remote Sens. Environ. 247. https://doi.org/10.1016/j.rse.2020.111942.

Liao, L.B., Weiss, S., Mills, S., Hauss, B., 2013. Suomi NPP VIIRS day-night band on-orbit performance. J. Geophys. Res. Atmos. 118, 12705–12718. https://doi.org/10.1002/2013JD020475.

Liu, Y., Wang, Z., Sun, Q., Erb, A.M., Li, Z., Schaaf, C.B., Zhang, X., Román, M.O., Scott, R.L., Zhang, Q., Novick, K.A., Syndonia Bret-Harte, M., Petroy, S., SanClements, M., 2017. Evaluation of the VIIRS BRDF, Albedo and NBAR products suite and an assessment of continuity with the long term MODIS record. Remote Sens. Environ. https://doi.org/10.1016/j.rse.2017.09.020.

Liu, A., Wei, Y., Yu, B., Song, W., 2019. Estimation of cargo handling capacity of coastal ports in China based on panel model and DMSP-OLS nighttime light data. Remote Sens. https://doi.org/10.3390/rs11050582.

Liu, Q., Sha, D., Liu, W., Houser, P., Zhang, L., Hou, R., Lan, H., Flynn, C., Lu, M., Hu, T., Yang, C., 2020a. Spatiotemporal patterns of COVID-19 impact on human activities and environment in mainland China using nighttime light and air quality data. Remote Sens. https://doi.org/10.3390/rs12101576.

Liu, L., Zhou, H., Lan, M., Wang, Z., 2020b. Linking Luojia 1-01 nightlight imagery to urban crime. Appl. Geogr. 125, 102267. https://doi.org/10.1016/j.apgeog.2020.102267.

Ma, T., Zhou, C., Pei, T., Haynie, S., Fan, J., 2014. Responses of Suomi-NPP VIIRS-derived nighttime lights to socioeconomic activity in Chinas cities. Remote Sens. Lett. https://doi.org/10.1080/2150704X.2014.890758.

Ma, M., Ge, W., Shi, K., 2020. Airport's throughput estimation using nighttime light data in China mainland. IEEE Geosci. Remote Sens. Lett. https://doi.org/10.1109/lgrs.2020.2999530.

McHardy, T.M., Zhang, J., Reid, J.S., Miller, S.D., Hyer, E.J., Kuehn, R.E., 2015. An improved method for retrieving nighttime aerosol optical thickness from the VIIRS Day/Night Band. Atmos. Meas. Tech. https://doi.org/10.5194/amt-8-4773-2015.

Miller, S.D., Turner, R.E., 2009. A dynamic lunar spectral irradiance data set for NPOESS/VIIRS day/night band night time environmental applications. IEEE Trans. Geosci. Remote Sens. https://doi.org/10.1109/TGRS.2009.2012696.

Miller, S.D., Mills, S.P., Elvidge, C.D., Lindsey, D.T., Lee, T.F., Hawkins, J.D., 2012. Suomi satellite brings to light a unique frontier of nighttime environmental sensing capabilities. Proc. Natl. Acad. Sci. U. S. A. https://doi.org/10.1073/pnas.1207034109.

Miller, S.D., Straka III, W.C., Mills, S.P., Elvidge, C.D., Lee, T.F., Solbrig, J.E., Walther, A., Heidinger, A.K., Weiss, S.C., 2013. Illuminating the capabilities of the suomi national polar-orbiting partnership (NPP) visible infrared imaging radiometer suite (VIIRS) Day/Night Band. Remote Sens. 5 (12), 6717–6766. https://doi.org/10.3390/rs5126717.

Miller, S.D., Straka III, W.C., Yue, J., Smith, S.M., Alexander, M.J., Hoffmann, L., Setvák, M., Partain, P.T., 2015. Upper atmospheric gravity wave details revealed in night glow satellite imagery. Proc. Natl. Acad. Sci. 112 (49), 6728–6735. https://doi.org/10.1073/pnas.1508084112.

Moreira, R.C., Galvão, L.S., 2010. Variation in spectral shape of urban materials. Remote Sens. Lett. https://doi.org/10.1080/01431161003692032.

Newell, P.T., Liou, K., Zhang, Y., Sotirelis, T., Paxton, L.J., Mitchell, E.J., 2014. OVATION Prime-2013: extension of auroral precipitation model to higher disturbance levels. Sp. Weather. https://doi.org/10.1002/2014SW001056.

Oda, T., Maksyutov, S., 2011. A very high-resolution (1km×1 km) global fossil fuel CO2 emission inventory derived using a point source database and satellite observations of nighttime lights. Atmos. Chem. Phys. https://doi.org/10.5194/acp-11-543-2011.

Ou, J., Liu, X., Li, X., Li, M., Li, W., 2015. Evaluation of NPP-VIIRS nighttime light data for mapping global fossil fuel combustion CO2 emissions: a comparison with DMSP-OLS nighttime light data. PLoS One. https://doi.org/10.1371/journal.pone.0138310.

Riggs, G.A., Hall, D.K., Román, M.O., 2017. Overview of NASA's MODIS and visible infrared imaging radiometer suite (VIIRS) snow-cover earth system data records. Earth Syst. Sci. Data. https://doi.org/10.5194/essd-9-765-2017.

Román, M.O., Stokes, E.C., 2015. Holidays in lights: tracking cultural patterns in demand for energy services. Earth's Futur. https://doi.org/10.1002/2014EF000285.

Román, M.O., Schaaf, C.B., Woodcock, C.E., Strahler, A.H., Yang, X., Braswell, R.H., Curtis, P.S., Davis, K.J., Dragoni, D., Goulden, M.L., Gu, L., Hollinger, D.Y., Kolb, T.E., Meyers, T.P., Munger, J.W., Privette, J.L., Richardson, A.D., Wilson, T.B., Wofsy, S.C., 2009. The MODIS (collection V005) BRDF/albedo product: assessment of spatial representativeness over forested landscapes. Remote Sens. Environ. https://doi.org/10.1016/j.rse.2009.07.009.

Román, M.O., Wang, Z., Sun, Q., Kalb, V., Miller, S.D., Molthan, A., Schultz, L., Bell, J., Stokes, E.C., Pandey, B., Seto, K.C., Hall, D., Oda, T., Wolfe, R.E., Lin, G., Golpayegani, N., Devadiga, S., Davidson, C., Sarkar, S., Praderas, C., Schmaltz, J., Boller, R., Stevens, J., Ramos González, O.M., Padilla, E., Alonso, J., Detrés, Y., Armstrong, R., Miranda, I., Conte, Y., Marrero, N., MacManus, K., Esch, T., Masuoka, E.J., 2018. NASA's black marble nighttime lights product suite. Remote Sens. Environ. https://doi.org/10.1016/j.rse.2018.03.017.

Román, M.O., Stokes, E.C., Shrestha, R., Wang, Z., Schultz, L., Sepúlveda Carlo, E.A., Sun, Q., Bell, J., Molthan, A., Kalb, V., Ji, C., Seto, K.C., McClain, S.N., Enenkel, M., 2019. Satellite-based assessment of electricity restoration efforts in Puerto Rico after Hurricane Maria. PLoS One. https://doi.org/10.1371/journal.pone.0218883.

Sánchez de Miguel, A., 2015. Spatial, Temporal and Spectral Variation of Light pollution and its sources: Methodology and Resources. Doctoral dissertation, Universidad Complutense de Madrid. https://doi.org/10.5281/zenodo.1289933.

Sánchez de Miguel, A., Kyba, C.C.M., Aubé, M., Zamorano, J., Cardiel, N., Tapia, C., Bennie, J., Gaston, K.J., 2019. Colour remote sensing of the impact of artificial light at night (I): the potential of the international Space Station and other DSLR-based platforms. Remote Sens. Environ. https://doi.org/10.1016/j.rse.2019.01.035.

Sanchez de Miguel, A., Kyba, C.C.M., Zamorano, J., Gallego, J., Gaston, K.J., 2020. The nature of the diffuse light near cities detected in nighttime satellite imagery. Sci. Rep. https://doi.org/10.1038/s41598-020-64673-2.

Schaaf, C.B., Gao, F., Strahler, A.H., Lucht, W., Li, X., Tsang, T., Strugnell, N.C., Zhang, X., Jin, Y., Muller, J.P., Lewis, P., Barnsley, M., Hobson, P., Disney, M., Roberts, G., Dunderdale, M., Doll, C., D'Entremont, R.P., Hu, B., Liang, S., Privette, J.L., Roy, D., 2002. First operational BRDF, albedo nadir reflectance products from MODIS. Remote Sens. Environ. https://doi.org/10.1016/S0034-4257(02)00091-3.

Schlundt, C., Kokhanovsky, A.A., Von Hoyningen-Huene, W., Dinter, T., Istomina, L., Burrows, J.P., 2011. Synergetic cloud fraction determination for SCIAMACHY using MERIS. Atmos. Meas. Tech. https://doi.org/10.5194/amt-4-319-2011.

Seaman, C.J., Miller, S.D., 2013. VIIRS captures aurora motions. Bull. Amer. Meteor. Soc., Nowcast 94 (10), 1491–1493. https://doi.org/10.1175/BAMS-D-12-00221.1.

Shao, X., Cao, C., Uprety, S., 2013. Vicarious calibration of S-NPP/VIIRS day-night band. In: Earth Observing Systems, XVIII. https://doi.org/10.1117/12.2023412.

Shao, X., Cao, C., Zhang, B., Qiu, S., Elvidge, C., Von Hendy, M., 2014. Radiometric calibration of DMSP-OLS sensor using VIIRS day/night band. In: Earth Observing Missions and Sensors: Development, Implementation, and Characterization, III. https://doi.org/10.1117/12.2068999.

Sharma, R.C., Tateishi, R., Hara, K., Gharechelou, S., Iizuka, K., 2016. Global mapping of urban built-up areas of year 2014 by combining MODIS multispectral data with VIIRS nighttime light data. Int. J. Digit. Earth. https://doi.org/10.1080/17538947.2016.1168879.

Shi, K., Huang, C., Yu, B., Yin, B., Huang, Y., Wu, J., 2014a. Evaluation of NPP-VIIRS nighttime light composite data for extracting built-up urban areas. Remote Sens. Lett. https://doi.org/10.1080/2150704X.2014.905728.

Shi, K., Yu, B., Huang, Y., Hu, Y., Yin, B., Chen, Z., Chen, L., Wu, J., 2014b. Evaluating the ability of NPP-VIIRS nighttime light data to estimate the gross domestic product and the electric power consumption of China at multiple scales: a comparison with DMSP-OLS data. Remote Sens. https://doi.org/10.3390/rs6021705.

Solbrig, J.E., Miller, S.D., Zhang, J., Grasso, L., Kliewer, A., 2020. Assessing the stability of surface lights for use in retrievals of nocturnal atmospheric parameters. Atmos. Meas. Tech. https://doi.org/10.5194/amt-13-165-2020.

Stokes, E.C., Seto, K.C., 2019. Characterizing urban infrastructural transitions for the sustainable development goals using multi-temporal land, population, and nighttime light data. Remote Sens. Environ. https://doi.org/10.1016/j.rse.2019.111430.

Straka, W., Kondragunta, S., Wei, Z., Zhang, H., Miller, S.D., Watts, A., 2021. Examining the economic and environmental impacts of covid-19 using earth observation data. Remote Sens. https://doi.org/10.3390/rs13010005.

Tan, B., Woodcock, C.E., Hu, J., Zhang, P., Ozdogan, M., Huang, D., Yang, W., Knyazikhin, Y., Myneni, R.B., 2006. The impact of gridding artifacts on the local spatial properties of MODIS data: implications for validation, compositing, and band-to-band registration across resolutions. Remote Sens. Environ. https://doi.org/10.1016/j.rse.2006.06.008.

Tong, K.P., Kyba, C.C.M., Heygster, G., Kuechly, H.U., Notholt, J., Kolláth, Z., 2020. Angular distribution of upwelling artificial light in Europe as observed by Suomi–NPP satellite. J. Quant. Spectrosc. Radiat. Transf. https://doi.org/10.1016/j.jqsrt.2020.107009.

Uprety, S., Cao, C., Gu, Y., Shao, X., Blonski, S., Zhang, B., 2019. Calibration improvements in S-NPP VIIRS DNB sensor data record using version 2 reprocessing. IEEE Trans. Geosci. Remote Sens. https://doi.org/10.1109/TGRS.2019.2927942.

Wang, W., Cao, C., 2016. Monitoring the NOAA operational VIIRS RSB and DNB calibration stability using monthly and semi-monthly deep convective clouds time series. Remote Sens. https://doi.org/10.3390/rs8010032.

Wang, Z., Schaaf, C.B., Chopping, M.J., Strahler, A.H., Wang, J., Román, M.O., Rocha, A.V., Woodcock, C.E., Shuai, Y., 2012. Evaluation of moderate-resolution imaging Spectroradiometer (MODIS) snow albedo product (MCD43A) over tundra. Remote Sens. Environ. https://doi.org/10.1016/j.rse.2011.10.002.

Wang, Z., Schaaf, C.B., Strahler, A.H., Chopping, M.J., Román, M.O., Shuai, Y., Woodcock, C.E., Hollinger, D.Y., Fitzjarrald, D.R., 2014. Evaluation of MODIS albedo product (MCD43A) over grassland, agriculture and forest surface types during dormant and snow-covered periods. Remote Sens. Environ. https://doi.org/10.1016/j.rse.2013.08.025.

Wang, J., Aegerter, C., Xu, X., Szykman, J.J., 2016. Potential application of VIIRS Day/Night Band for monitoring nighttime surface PM2.5 air quality from space. Atmos. Environ. https://doi.org/10.1016/j.atmosenv.2015.11.013.

Wang, Z., Román, M.O., Sun, Q., Molthan, A.L., Schultz, L.A., Kalb, V.L., 2018a. Monitoring disaster-related power outages using nasa black marble nighttime light product. In: International Archives of the Photogrammetry, Remote Sensing and Spatial Information Sciences - ISPRS Archives. https://doi.org/10.5194/isprs-archives-XLII-3-1853-2018.

Wang, Z., Schaaf, C.B., Sun, Q., Shuai, Y., Román, M.O., 2018b. Capturing rapid land surface dynamics with collection V006 MODIS BRDF/NBAR/Albedo (MCD43) products. Remote Sens. Environ. https://doi.org/10.1016/j.rse.2018.02.001.

Wang, X., Mu, X., Yan, G., 2020. Quantitative analysis of aerosol influence on Suomi-NPP VIIRS nighttime light in China. IEEE J. Sel. Top. Appl. Earth Obs. Remote Sens. https://doi.org/10.1109/jstars.2020.3003480.

Wang, J., Roudini, S., Hyer, E.J., Xu, X., Zhou, M., Garcia, L.C., Reid, J.S., Peterson, D.A., da Silva, A.M., 2020a. Detecting nighttime fire combustion phase by hybrid application of visible and infrared radiation from Suomi NPP VIIRS. Remote Sens. Environ. https://doi.org/10.1016/j.rse.2019.111466.

Wang, J., Zhou, M., Xu, X., Roudini, S., Sander, S.P., Pongetti, T.J., Miller, S.D., Reid, J.S., Hyer, E., Spurr, R., 2020b. Development of a nighttime shortwave radiative transfer model for remote sensing of nocturnal aerosols and fires from VIIRS. Remote Sens. Environ. https://doi.org/10.1016/j.rse.2020.111727.

Wei, S., Fang, H., 2016. Estimation of canopy clumping index from MISR and MODIS sensors using the normalized difference hotspot and darkspot (NDHD) method: the influence of BRDF models and solar zenith angle. Remote Sens. Environ. https://doi.org/10.1016/j.rse.2016.10.039.

Witmer, F.D.W., 2015. Remote sensing of violent conflict: eyes from above. Int. J. Remote Sens. https://doi.org/10.1080/01431161.2015.1035412.

Wolfe, R.E., Lin, G., Nishihama, M., Tewari, K.P., Tilton, J.C., Isaacman, A.R., 2013. Suomi NPP VIIRS prelaunch and on-orbit geometric calibration and characterization. J. Geophys. Res. Atmos. https://doi.org/10.1002/jgrd.50873.

Wu, J., He, S., Peng, J., Li, W., Zhong, X., 2013. Intercalibration of DMSP-OLS nighttime light data by the invariant region method. Int. J. Remote Sens. https://doi.org/10.1080/01431161.2013.820365.

Xie, Y., Weng, Q., Fu, P., 2019. Temporal variations of artificial nighttime lights and their implications for urbanization in the conterminous United States, 2013–2017. Remote Sens. Environ. https://doi.org/10.1016/j.rse.2019.03.008.

Xiong, X., Butler, J., Chiang, K., Efremova, B., Fulbright, J., Lei, N., McIntire, J., Wang, Z., 2014. VIIRS on-orbit calibration and performance update. In: International Geoscience and Remote Sensing Symposium (IGARSS), pp. 1389–1392. https://doi.org/10.1109/IGARSS.2014.6946694.

Yan, W.Y., Shaker, A., El-Ashmawy, N., 2015. Urban land cover classification using airborne LiDAR data: a review. Remote Sens. Environ. https://doi.org/10.1016/j.rse.2014.11.001.

Yu, H., Kaufman, Y.J., Chin, M., Feingold, G., Remer, L.A., Anderson, T.L., Balkanski, Y., Bellouin, N., Boucher, O., Christopher, S., DeCola, P., Kahn, R., Koch, D., Loeb, N., Reddy, M.S., Schulz, M., Takemura, T., Zhou, M., 2006. A review of measurement-based assessments of the aerosol direct radiative effect and forcing. Atmos. Chem. Phys. https://doi.org/10.5194/acp-6-613-2006.

Yu, B., Shi, K., Hu, Y., Huang, C., Chen, Z., Wu, J., 2015. Poverty evaluation using NPP-VIIRS nighttime light composite data at the county level in China. IEEE J. Sel. Top. Appl. Earth Obs. Remote Sens. https://doi.org/10.1109/JSTARS.2015.2399416.

Zeng, X., Li, C., 2019. The influence of heterogeneity on lunar irradiance based on multiscale analysis. Remote Sens. https://doi.org/10.3390/rs11222696.

Zeng, X., Shao, X., Qiu, S., Ma, L., Gao, C., Li, C., 2018. Stability monitoring of the VIIRS day/night band over dome C with a lunar irradiance model and BRDF correction. Remote Sens. https://doi.org/10.3390/rs10020189.

Zhang, J., Reid, J.S., Miller, S.D., Turk, F.J., 2008. Strategy for studying nocturnal aerosol optical depth using artificial lights. Int. J. Remote Sens. https://doi.org/10.1080/01431160802020528.

Zhang, Q., Schaaf, C., Seto, K.C., 2013. The vegetation adjusted NTL urban index: a new approach to reduce saturation and increase variation in nighttime luminosity. Remote Sens. Environ. https://doi.org/10.1016/j.rse.2012.10.022.

Zhang, Q., Pandey, B., Seto, K.C., 2016. A robust method to generate a consistent time series from DMSP/OLS nighttime light data. IEEE Trans. Geosci. Remote Sens. https://doi.org/10.1109/TGRS.2016.2572724.

Zhang, J., Jaker, S.L., Reid, J.S., Miller, S.D., Solbrig, J., Toth, T.D., 2019. Characterization and application of artificial light sources for nighttime aerosol optical depth retrievals using the visible infrared imager radiometer suite day/night band. Atmos. Meas. Tech. https://doi.org/10.5194/amt-12-3209-2019.

Zhao, X., Yu, B., Liu, Y., Yao, S., Lian, T., Chen, L., Yang, C., Chen, Z., Wu, J., 2018. NPP-VIIRS DNB daily data in natural disaster assessment: evidence from selected case studies. Remote Sens. https://doi.org/10.3390/rs10101526.

Zhao, M., Zhou, Y., Li, X., Zhou, C., Cheng, W., Li, M., Huang, K., 2020. Building a series of consistent night-time light data (1992-2018) in Southeast Asia by integrating DMSP-OLS and NPP-VIIRS. IEEE Trans. Geosci. Remote Sens. https://doi.org/10.1109/TGRS.2019.2949797.

Zheng, Q., Weng, Q., Wang, K., 2019. Developing a new cross-sensor calibration model for DMSP-OLS and Suomi-NPP VIIRS night-light imageries. ISPRS J. Photogramm. Remote Sens. https://doi.org/10.1016/j.isprsjprs.2019.04.019.

Zheng, Q., Weng, Q., Wang, K., 2020. Correcting the pixel blooming effect (PiBE) of DMSP-OLS nighttime light imagery. Remote Sens. Environ. https://doi.org/10.1016/j.rse.2020.111707.

Zhou, Y., Smith, S.J., Elvidge, C.D., Zhao, K., Thomson, A., Imhoff, M., 2014. A cluster-based method to map urban area from DMSP/OLS nightlights. Remote Sens. Environ. https://doi.org/10.1016/j.rse.2014.03.004.

Zhou, H., Liu, L., Lan, M., Yang, B., Wang, Z., 2019. Assessing the impact of nightlight gradients on street robbery and burglary in Cincinnati of Ohio State, USA. Remote Sens. https://doi.org/10.3390/rs11171958.

Zhu, Z., Wang, S., Woodcock, C.E., 2015. Improvement and expansion of the Fmask algorithm: cloud, cloud shadow, and snow detection for Landsats 4-7, 8, and sentinel 2 images. Remote Sens. Environ. https://doi.org/10.1016/j.rse.2014.12.014.